Characterization and differentiation of rock varnish types from different environments by microanalytical techniques

D. S. Macholdt[1,2*], K. P. Jochum[2], C. Pöhlker[1], A. Arangio[3], J.-D. Foerster[1], B. Stoll[2], U. Weis[2], B. Weber[3], M. Müller[4], M. Kappl[4], M. Shiraiwa[3,5], A. L. D. Kilcoyne[6], M. Weigand[7], D. Scholz[8], G. Haug[2], A. Al-Amri[9], and M. O. Andreae[1,9]

1. Biogeochemistry Department, Max Planck Institute for Chemistry, Mainz, Germany.
2. Climate Geochemistry Department, Max Planck Institute for Chemistry, Mainz, Germany.
3. Multiphase Chemistry Department, Max Planck Institute for Chemistry, Mainz, Germany.
4. Physics of Interfaces Department, Max Planck Institute for Polymer Research, Mainz, Germany.
5. Department of Chemistry, University of California, Irvine, CA, USA.
6. Lawrence Berkeley National Laboratory, Berkeley, CA, United States.
7. Modern Magnetic Systems Department, Max Planck Institute for Intelligent Systems, Stuttgart, Germany.
8. Geology Department, Johannes Gutenberg University, Mainz, Germany.
9. Geology and Geophysics Department, King Saud University, Riyadh, Saudi Arabia.

(*correspondence: d.macholdt@mpic.de, P.O. Box 3060, 55020 Mainz, Germany, +49(6131)-305 6705)

Submitted to Geochimica et Cosmochimica Acta (GCA)

Keywords: rock varnish, Varnish Types, desert varnish, fs LA-ICP-MS, EPR, SEM, STXM-NEXAFS, categorization

Abstract

We investigated rock varnishes collected from several locations and environments worldwide by a broad range of microanalytical techniques. These techniques were selected to address the challenges posed by the chemical and structural complexity within the micrometer- to nanometer-sized structures in these geological materials. Femtosecond laser ablation-inductively coupled plasma-mass spectrometry (fs LA-ICP-MS), scanning transmission X-ray microscopy-near edge X-ray adsorption fine structure spectroscopy (STXM-NEXAFS) in combination with scanning electron microscopy (SEM) of focused ion beam (FIB) ultra-thin (100-200 nm) sections, conventional and polarization microscopy, as well as electron paramagnetic resonance (EPR) measurements were used to obtain information about these rock varnishes.

Rock varnishes, which cannot readily be distinguished based on their macroscopic appearance, differ significantly in their constituent elemental mass fractions, e.g., of Mn, Fe, Ni, Co, Ba, and Pb, and their rare earth element (REE) patterns. Structural characteristics, such as the particle sizes of embedded dust grains, internal structures such as layers of Mn-, Fe-, and Ca -rich material, and structures such as cavities varied between varnishes from different environments and regions in the world. The EPR spectra were consistent with aged biogenic Mn oxides in all samples, but showed subtle differences between samples of different origin.

Our observations allow us to separate rock varnishes into different types, with differences that might be indicators of distinct geneses. Five different types of rock varnish could be distinguished, Type I – V, of which only Type I might be useful as potential paleoclimate archive. Each varnish type has specific characteristics in terms of their elemental composition, element distribution, and structures. The combination of element ratios (Mn/Ba, Al/Ni, Mn/REY, Mn/Ce, Mn/Pb, La_N/Yb_N, and Ce/Ce*), total REE contents, and structures can be used to separate the different types of rock varnish from each other.

1. Introduction

Rock varnishes are black layers of unknown geneses, occurring on rock surfaces of slowly weathering rocks, independent of the lithology of the underlying rock (Engel and Sharp, 1958). They consist of poorly crystallized Mn and Fe oxides, as well as clay minerals (Potter and Rossman, 1979). The clay mineral fraction, which is thought to be derived from dust, represents up to 70% of the varnish volume (Thiagarajan and Lee, 2004) and is cemented together by a nanocrystalline matrix of Mn- and Fe-oxides and hydroxides. The origin and precipitation of the Mn-rich matrix material is not fully understood, but it has most likely dust as element source, from which Mn and other constituents of the varnish have been leached before the dust particles are removed again by wind erosion (Hodge et al., 2005; Nowinski et al., 2013; Thiagarajan and Lee, 2004). While the upper continental crust has a mass fraction of about 0.1 % MnO (Rudnick and Gao, 2003), varnish is strongly enriched (40-200 times) in this element. Rock varnish deposited in the form of a layered sediment is potentially applicable as paleoclimate archive (Dorn, 1984).

The first description of rock varnish in 1812 was written by the so-called father of rock varnish, Alexander von Humboldt (Dorn, 2008; Von Humboldt and Bonpland, 1819), who observed it in the splash zone at the cataracts of the Orinoco River. He was aware that similar rock varnishes can be found in a wide variety of terrestrial environments. Currently, biological and abiotic processes, as well as a combination of both, have been suggested for the genesis of rock varnish, but none could be definitely proven by now (Dorn, 2009).

There are three main theories how varnish could form (Dorn, 2008): I) By abiogenic precipitation under the right pH (5.7) and Eh (0.8) conditions of rainwater or dew to geochemically fractionate Mn (Thiagarajan and Lee, 2004). In this way, Mn can be enriched without simultaneous enrichment of Fe. However, this process is very slow and the question remains why varnish covers only certain patches and not large areas. II) By biologically induced or controlled varnish growth. Here, the Mn oxyhydroxide mineralization is either the result of interactions between biological membrane/cell surfaces and the inorganic environment, or cellular activities provide the initial nucleation of the Mn oxyhydroxides, followed by the growth of the mineral product (Northup et al., 2010; Perry et al., 2004; Perry and Kolb, 2004; Perry et al., 2005). Biogenic Mn oxidation is a fast process compared to abiogenic oxidation, which raises the question why some varnishes grow only nanometers per decade. III) By a combination of the processes described above.

The general structure of Mn oxides and hydroxides, called Mn oxyhydroxides for simplification, is based on octahedrally coordinated Mn ions, which have the ability to be stacked in several different ways and build sheet, chain, and tunnel structures. Which oxyhydroxide mineral forms depends on several factors, such as pH, Eh, temperature, biological mediation, and cation availability (Tebo et al., 2004). Biologically mediated Mn oxyhydroxides will be called bio-oxides in the following. Manganese minerals, which are often quite small or even nanocrystalline, are known for their large surface areas and negative charges due to non-shared oxygen atoms at the surfaces. Vacancies, reduced valence states of Mn, or isomorphic substitution of lower valence state elements for Mn add additional negative charge, which can be balanced by cation absorption. These structural properties make manganese oxyhydroxides well-known but poorly understood ad- and absorbants.

Estimates of the growth rate of rock varnish vary between 1 and 40 µm per 1000 a (Liu and Broecker, 2000; Spilde et al., 2013) but growth might be much faster in non-arid environments. The growth rate seems to depend on the humidity of the environment, with slower growth rates for desert climates (Krinsley et al., 2012). The maximum thickness of rock varnish is about 250 µm (Northup et al., 2010), but the values are controversial. Commonly found thicknesses are in the range of 50 µm (Raymond et al., 1993). Rock varnish is thought to be suitable as correlative dating tool for desert environments, usable beyond ^{14}C dating (Broecker and Liu, 2001). Unfortunately, no direct dating of rock varnish has yet been successful (Watchman, 2000), but a maximal age can be given by knowing the exposure age of the host rock or varnished surface (Lee and Bland, 2003).

Many studies on varnish and its chemical composition have been published (Dorn, 2008; Goldsmith et al., 2014; Reneau et al., 1992; Thiagarajan and Lee, 2004), and most publications describe arid desert varnish. However, some authors also discuss samples from more humid areas (Krinsley et al., 2012), urban areas (Vicenzi, 2016), cold environments (Dorn et al., 1992), cave samples (Spilde et al., 2002), or even extraterrestrial sites (DiGregorio, 2001; Lanza et al., 2012; Perry and Sephton, 2006). All of these samples fall under the term “rock varnish”. However, it is problematic that data from all types of varnishes, independent of region and environment, are used indiscriminately to explain varnish formation as a single common phenomenon, which might originate from different formation processes. This might result in incorrect conclusions and therefore prevent us from gaining an insight into a mystery that has puzzles scientists for over 200 years. In this study we therefore compare typical arid desert varnish, which can be useful for future regional paleoclimate reconstruction (Dorn, 1984), to varnishes from several regions and environments worldwide.

The categorization into different varnish types was approached by using different microanalytical techniques. Femtosecond LA-ICP-MS was used to provide major-, minor-, and trace element information to gain a geochemical “varnish fingerprint”, STXM-NEXAFS was chosen to visualize nanostructures and element distributions on FIB milled ultra-thin sections (100-200 nm), electron paramagnetic resonance (EPR) spectroscopy was applied to investigate the Mn oxyhydroxide matrix, and SEM of FIB slices was utilized to visualize cavities and layered and disordered nanostructures.

In EPR spectroscopy, species with unpaired electrons immersed in a magnetic field can absorb energy from microwave radiation. ^{55}Manganese and ^{57}Fe contained in rock varnish are magnetically active and are the main contributors to the EPR signals, which are characterized by an unstructured and broad peak and linewidth. Kim et al. (2011) proposed that manganese bio-oxides produce EPR spectral signatures different from those formed by abiogenic and synthetic processes. In their study, they observed a considerably narrower linewidth (< 560 G) for biogenic samples than for abiogenic Mn oxide minerals, which have a 2-6 times broader (> 1200 G) linewidth. These narrow linewidths of Mn bio-oxide minerals are unique for pure Mn oxides, since they are usually only observed for highly diluted samples, e.g., 0.5% m/m Mn ions supported on alumina (Kijlstra et al., 1997). Kim et al. (2011) explained the narrow linewidths with high amounts of layer site vacancies (15-50%), small particle sizes, and the absence or lack (0-5%) of Mn^{3+} in Mn bio-oxides. Furthermore, they investigated rock varnish to see into which category, biogenic or abiogenic it falls, and observed an intermediate linewidth between 600 and 1200 G for their samples. This was explained by an originally biogenic origin, followed by an abiogenic transformation from birnessite to todorokite during aging processes, a common transformation process based on observations from Mn nodules by Tebo et al. (2005). Biogenic layered Mn oxides may partially transform to tunnel structure minerals and/or acquire cations with aging, filling up vacancies (Tebo et al., 2004). Kim et al. (2011) chose for their investigations a rock varnish sample from Four Buttes, Mojave Desert, CA, USA. In our paper, we interpret our EPR dataset on basis of their observations and interpretation.

2. Samples

Several different environments were studied (Fig. A in the appendix):

1. Arid desert environments in California (USA), Mauritania, and Saudi Arabia. These samples are compared to previously investigated arid desert varnishes from California and Israel (Macholdt et al., 2015). In California, the additional samples studied here were collected in the Anza Borrego desert (part of the Colorado desert) and in Johnson Canyon in the Mojave Desert, the driest desert in North America. In Saudi Arabia, they were collected near Jubbah and on Jebel Yatib, both within the An Nafud desert. In Mauritania, samples were taken in a canyon northwest of Azougui, within the Sahara region. The previously studied samples had been collected from different locations in the Mojave Desert and Sde Boker within the Negev Desert in Israel. All of these samples will be assigned to the term Type I varnish in the following.
2. Semi-arid desert environments in the Chihuahuan Desert, Texas, and the Sonoran Desert, Arizona. This type of varnish, in the following called Type II, differs from Type III varnish by its typical rock varnish appearance, i.e., full coverage of the rock surfaces. It covers larger surfaces on the top and sides of rock outcrops, without visible growth directions. It differs from typical arid desert varnishes (Type I) by its mostly thicker crusts an the growth features without detectable layering.
3. Semi-arid desert or coastal desert environments in the Knersvlakte, South Africa. Previously collected and investigated samples from South Africa (Macholdt et al., 2015) will be referred to as SA-1 in the following text, the new samples as SA-2. This type of varnish, called Type III in the following, differs from the Type II semi-arid desert varnish (described above) by its growth direction and appearance. The South African samples grew on host rock pebbles of a few centimeters in di-

ameter. Round patches of pebbles within the desert, of about 1-10 m in diameter, were colored dark black to brown. The pebbles in the middle of the patches show a black varnish crust with metallic luster on their top and a slightly duller tinge on the subsoil part and sides, the pebbles closer to the rim were dull brown. The top and bottom sides of the rocks were often not fully enclosed by the varnish, which appears to have grown from the rock-soil-atmosphere contact upwards and downwards on the rock surface, and therefore also within the subsoil.

4. Urban environments with varnishes on sandstone buildings, e.g., varnish from the Smithsonian Castle, Washington, D.C., USA (Vicenzi, 2016) and the Freiburger Münster, Freiburg, Germany. This varnish seems to grow preferentially on sandstone buildings. At the Freiburger Münster, varnish was found up to a height of about 8 m, all black patches above this height were significantly less Mn-rich and are probably soot or fungi covered areas. This varnish will be called Type IV in the following.
5. River splash zones, e.g., from the Erie Barge Canal, close to Middleport, and the Adirondack Raquette River, close to South Colton. Both sampling sites are located in New York State, USA (Krinsley et al., 2012), an area with about 1028 mm of annual precipitation. The rock varnish sample from Erie Barge canal is ≤ 100 years old. These varnishes will be called Type V varnish in the following.

All rock varnish samples from California and South Africa were taken from the ground, and have therefore pebbles and small rocks (a few to tens of centimeters) as host rocks, which had direct contact with the underlying soil. The Israeli, Texan, Arizonian, Mauritanian, and Saudi Arabian samples were collected as fragments or chips from larger boulders or outcrops (meters in diameter). Type IV varnish from the Freiburger Münster was collected as a mm-size chip from the church wall, at a height of about 0.5 m from the ground. The Smithsonian Castle varnish was taken from the castle wall at a height of about 2 m. Type V varnishes were taken from boulders within the river splash zone. Regarding the fs LA-ICP-MS measurements, 9-16 different spots were investigated on each sample. For FIB and SEM investigations, three samples from California (2x Death Valley, 1x Johnson Canyon; Type I varnish), four samples from South Africa (2x SA-1, 2x SA-2; Type III varnish), one sample from Israel (Type I varnish), two samples from Saudi Arabia (1x Jubbah, 1x Yatib; Type I varnish), one sample from NY state (Erie Barge Canal; Type V varnish), two urban varnish samples (1x Smithsonian Castle, 1x Freiburger

Münster; Type IV varnish), and one sample from Texas (Type II varnish) were chosen. Table 1 in the appendix lists the specimens used for the analyses together with information about the sampling locations.

Dust samples were collected underneath Type I varnished rocks in the Anza Borrego Desert and the Mojave Desert (both within CA, USA) and in Jubbah and Yatib (both within the An Nafud, Saudi Arabia). Furthermore, dust grains accumulated on top of varnished rocks were collected in Sde Boker (Negev, Israel). For Type III varnish, dust underneath varnished rocks was collected in the Knersvlakte, South Africa.

2.1 Sample preparation

Thick sections (about 70 µm thick) were prepared for fs LA-ICP-MS measurements. Polishing was avoided to exclude trace element contamination from the polishing material. The roughness of the unpolished surfaces can be neglected for fs LA-ICP-MS measurements, since a pre-ablation step prior to each measurement produced almost flat surfaces, and correction by an internal standard element, Al, was performed. The varnish coatings were cut perpendicular to the surfaces, whereby cross-sections through the sedimentation sequence of the varnishes were exposed, similar to the procedure described by Reneau et al. (1992). All thick section samples were enclosed by resin (EpoxiCure ™2 Resin and Hardener from Buehler) prior to thinning.

For desert dust measurements, the dust samples were sieved, grains <50 µm were directly mounted on double-adhesive tape, and mineral grains >50 µm were ground to grain sizes <100 µm, prior to mounting. These mounts were measured as line-ablations by fs LA-ICP-MS.

Ultra-thin FIB slices, comparable to those produced from rock varnish by Krinsley et al. (2013), were milled to sizes of about 50 x 30 µm and thicknesses of about 100-200 nm to perform X-ray micro-spectroscopy in transmission light mode. For this purpose, suitable areas for preparation were selected by a combination of microscopy and scanning electron microscopy (SEM). Furthermore, SEM images of the ultra-thin sections were used for structure investigations.

The EPR spectroscopy measurements were carried out on varnish powders of five samples (CA-JC, CA-AB, AR-Y, SA-2, IS). The powders were produced by taking off the upper layer of varnish from the host rock, using a mechanical abrasion instrument from the manufacturer DREMEL. From each sample, 1 g of material was collected and 11 mg were used for the actual analyses. The material was prepared on filters, which were used for both, room temperature (RT) and 90 K experiments.

3. Analytical methods

3.1 Imaging and underlying rock identification

A Leica DM RX polarizing microscope was used for investigations of varnish structures in thick sections (about 70 µm), and to check ablated line scans by LA-ICP-MS subsequent to the analysis. The host rock types were determined based on thin section observations using polarization microscopy. During the FIB slice preparation, slices were visualized by SEM. These SEM images give insights into the nanometer structures, growth features, and grain- and cavity-distributions within the varnishes.

3.2 Femtosecond laser ablation-inductively coupled plasma-mass spectrometry

Measurements were carried out at the Max Planck Institute for Chemistry (Mainz, Germany). A ThermoFisher Element 2 single-collector sector-field ICP-mass spectrometer was combined with an ESI 200 nm fs laser ablation system NWRFemto. Important parameters of the ICP-MS and the laser are listed in Tables 2 and 3 in the appendix. Laser ablation was conducted in a New Wave Large Format Cell in a He atmosphere. This carrier gas was mixed with an Ar gas flow to transport the aerosols generated by ablation to the ICP-MS.

All measurements were conducted in medium mass resolution mode (2000) with flat top peaks, since in this way many oxides and molecules from Ar and O produced in the plasma can be separated from the atomic ions, e.g., $^{40}Ar^{14}N^{1}H^{+}$ can be separated from ^{55}Mn, giving an improvement of the signal to blank ratio for many elements.

After pre-ablation, each sample was scanned along a profile from the underlying rock through the varnish into the embedding resin. The varnish region was defined by a high (≥ 2%) MnO_2 abundance. This value was chosen, since values lower than 2 % are usually mixtures of varnish and host rock, based on the comparison of Mn mass fraction results to ablated line patterns on thick sections. At the varnish-rock interface, the Mn signal drops abruptly to values below 2% MnO_2. To obtain a representative bulk analysis for the varnishes, the concentrations for each element were averaged over the full varnish profile between the host rock contact and the resin. Bulk analyses were performed for the major elements (Na, Mg, Al, Si, P, K, Ca, Ti, Mn, and Fe) and 30 trace elements (isotopes used and all measurement results are listed in Table 4 of the appendix). The element concentrations were determined by measuring the ion intensities of the elements of interest using Al as the internal standard element, analogous to Goldsmith et al. (2014). Since no suitable microanalytical varnish reference material existed until recently (Jochum et al., 2016; Macholdt et al., 2016), the homogeneous GSE-1G glass (GeoReM database http://georem.mpch-mainz.gwdg.de) was used for calibration. This was possible, since fs LA-ICP-MS allows nearly matrix-independent calibration (Jochum et al., 2014). To normalize the data, the oxides of the major elements (Na_2O, MgO, Al_2O_3, SiO_2, P_2O_5, K_2O, CaO, TiO_2, MnO_2, and Fe_2O_3) were assumed to add up to 98 % m/m. By this method, the procedure is reproducible and easily recalculated if future measurements can provide the exact amount of water and organics within the rock varnish.

Furthermore, dust collected adjacent to the varnish samples was measured by fs LA-ICP-MS. The method, detection limits, measurement parameters, and tape blanks are described in detail in Macholdt et al. (2014). The dust grains and the powder reference material T1-G (GeoReM database http://georem.mpch-mainz.gwdg.de) were mounted on double-adhesive tape, which was attached to a pure Ir strip prior to measuring.

3.3 Electron paramagnetic resonance analysis

Measurements were carried out at the Max Planck Institute for Chemistry (Mainz, Germany). A CW-EPR (Continuous Wave) model EMX-plus from Bruker was used for the measurements. The powdered rock varnish material was prepared on a Teflon membrane filter from Merck Millipore (Reference number JVWP04700), which was folded and inserted into a glass tube prior to introducing it in the EPR instrument. For the experiments at 90 K, the system was cooled by liquid nitrogen vapor stream. The temperature was carefully monitored by the EPR software and an additional thermometer for verification. The frequency used was 9.837440 GHz for room temperature experiments (RT, about 293 K) and 9.418697 GHz for 90 K measurements, the magnetic field was scanned from 0 to 6000 Gauss. For each sample and temperature, the EPR spectra were recorded at eleven different microwave radiation powers, sweeping between 0.22 and 224 mW to study the saturation behavior of the signal. Further instrumental parameters were: modulation amplitude, 3.0 G; modulation frequency, 100 kHz; conversion time, 30 ms; time constant, 0.01 ms; sweep time, 300 s; number of scans, 1.

3.4 Scanning transmission X-ray microscopy-near edge X-ray adsorption fine structure spectroscopy and focused ion beam sputtering

Focused ion beam (FIB) sputtering (milling) was performed at the Max Planck Institute for Polymer Research (Mainz, Germany) using a Nova600Nanolab FIB dual-beam instrument of FEI. Simultaneously, SEM microscopy was applied to carefully determine and monitor the site of milling. Micro-basins were located by microscopy and used for the preparation of the 50 x 30 µm FIB slices. The entire samples were sputtered with 50 nm of Pt using a Baltec MED020 sputtering equipment. The selected preparation sites were coated with an additional, approximately 2 µm thick Pt layer using beam-induced Pt deposition from a metallo-organic precursor gas (1 nA at 30 kV). Milling was performed by Ga^+-ion sputtering with a resolution of about 10 nm. In a first milling step (20 nA, 30 kV), two trenches on both sides of the Pt deposition were created, followed by a second milling step at lower beam currents (7 nA and 5 nA at 30 kV) to obtain flat surfaces of the pre-thinned, about 1 µm thick, lamella. The thinned samples were lifted out and transferred to a TEM grid onto which they were attached with Pt. Stepwise thinning and polishing (1 nA and 0.5 nA at 30 kV) produced FIB slices with thicknesses of about 100-200 nm. These ultra-thin sections and the transfer onto a TEM grid are necessary for transmission measurements by the STXM-NEXAFS.

The STXM-NEXAFS analyses were conducted using soft X-ray synchrotron light and two X-ray microscopes: I) the instrument at beamline 5.3.2.2 (Kilcoyne et al., 2003) at the Advanced Light Source (Kim et al.), Berkeley, CA, USA, and II) the MAXYMUS microscope at beamline UE46-PGM-2 (Follath et al., 2010) at the synchrotron BESSY II, Helmholtz-Zentrum Berlin, Germany. Both STXM instruments are equipped with a high energy resolving grating (resolving power at the carbon K-edge: ALS $E/\Delta E \leq 5000$; BESSY II: $E/\Delta E \leq 8000$), a Fresnel zone plate, providing a spatial resolution of about 30 nm, and phosphor-coated Lucite photomultiplier tubes for the detection of transmitted photons. At the ALS, the measurement chamber was filled with a He atmosphere prior to measuring, whereas at BESSY the measurements were conducted in a vacuum. In this study, STXM-NEXAFS elemental maps of Fe, Mn, and Ca are presented, which were recorded as images produced at discrete energies. For calibration, the characteristic pi resonance peak at 285.2 eV was measured before each measurement session. The data were evaluated with the Interactive Data Language (IDL) widget “Analysis of X-ray microscopy Images and Spectra” (aXis2000) and IGOR Pro.

4. Results

4.1 Scanning electron microscopy images and structures

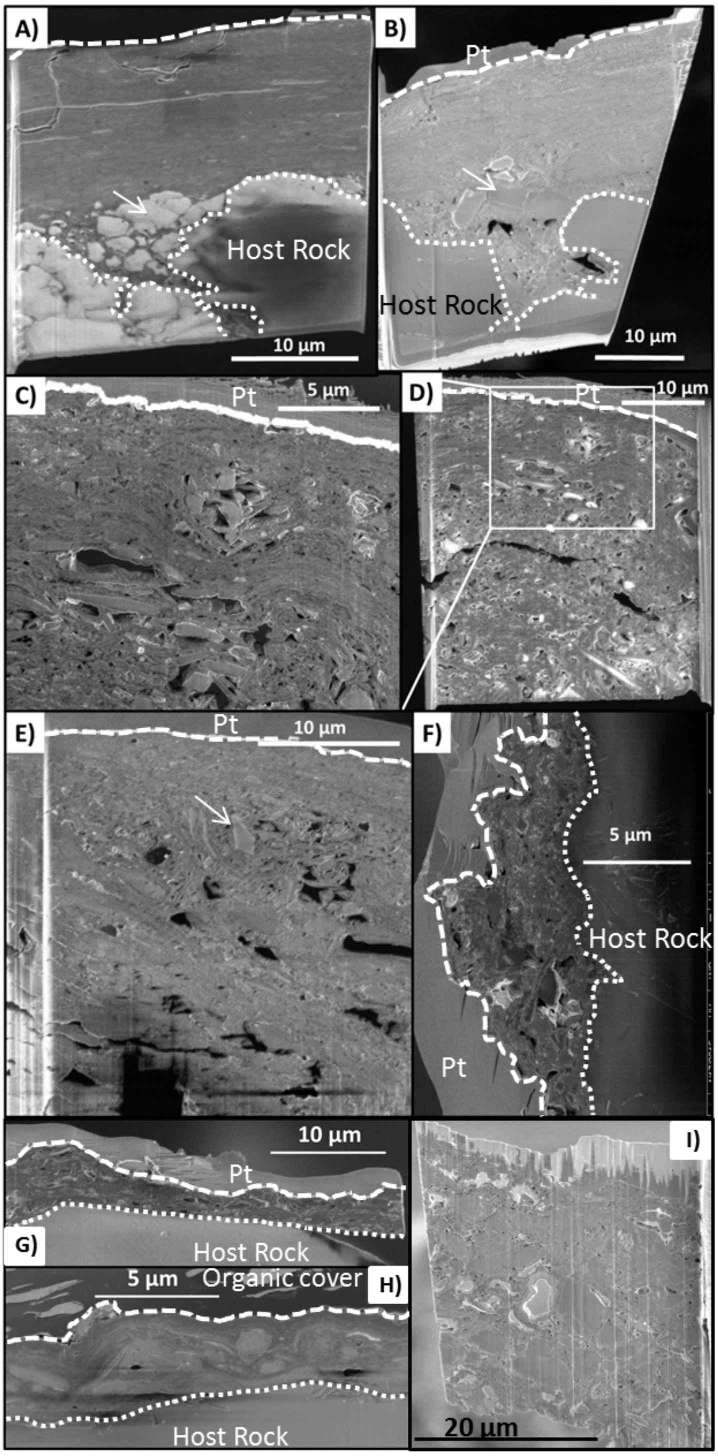

Figure 1: SEM images of five ultra-thin (100-200 nm) transections. All SEM images were produced by an FIB instrument with an accelerating voltage between 2 and 5 kV. A) Type I varnish, Saudi Arabia (AR14 Y1), B) Type I varnish, California (CA WS18), C) close-up of D), D) Type III varnish, South Africa (SA13 mM-f), E) Type I varnish, Saudi Arabia (AR14 J1), F) Type IV varnish, Washington D.C. (SC, castle west facade). G) Type V varnish, NY State (E

Canal), H) Type IV varnish, Germany (FM), and I) Type II varnish, Texas (TX). All FIB slices had been coated on their top side by Pt. Host rock-to-varnish and varnish-to-Pt boundaries are marked by white, dashed lines.

Significantly denser packing and smaller dust grains can be observed in layered varnishes (Fig. 1 A, B) compared to other unstructured ones (Fig. 1 C-H). These fine-grained layers were only found in Type I varnishes. However, at the contact from matrix and dust to the underlying rock, the layered varnish structure becomes disordered and cavities are present. The rock at the rock-varnish interface appears to have broken up prior or contemporaneous to growing or depositing. Either these rock fragments were broken off and dragged upwards until they were incorporated into the structure (Fig. 1 B, arrow), or the underlying rock was dissolved after evolving a varnish cover, and the developed crack system was filled up by unstructured varnish material (Fig. 1 A, arrow). However, not all Type I varnishes show layers. The Saudi Arabian varnish from Jubbah, collected only 110 km away from the arid desert varnish location in Yatib, shows a disordered structure with large (up to 1 µm), sometimes angular, mineral fragments (Fig. 1 E, arrow). This structure is very similar to those observed in Type II, III, and IV varnishes. Those varnish types show no plane layers parallel to the underlying rock, but exhibit large angular cavities and mineral grains. These cavities seem to be the result of loose packing and fast growth around the grains (Fig. 1 C-F, I). Sheets of matrix material often bend around mineral dust packages and incorporate them thereby into their botryoidal structure (Fig. 1 C, E). The ellipsoidal cavities (about 1 µm in diameter) might be an indicator for Mn oxyhydroxide growth around organisms, but this cannot be proven with the current methods at hand.

The structures of the two Type IV varnishes seem to differ significantly from each other, even though they were both sampled from sandstone buildings. The sample from the Smithsonian Castles western facade (SC) shows a disordered structure with large particles and cavities (Fig 1 F), whereas the Freiburger Münster (FM) sample shows parallel layers with almost no cavities, incorporating large (~1 µm) round features that are overgrown by layers, resulting in a partially botryoidal structure (Fig 1 H). The Type V varnish structure resembles the Type III varnish structure, but no mineral grains can be observed in the SEM images of the former (Fig. 1 G).

Figure B in the appendix shows close-up reflected light microscopy images (B-(A-D)) and transmission light polarization microscopy images (B-(E, F)), which were taken to explain the differences between the SEM appearance of AR-Y (Fig. 1 B) and AR-J (Fig. 1 E). Larger mineral grains and a significant topography can be observed in the Saudi Arabian sample from Jubbah, which are absent in the varnish sample collected in Yatib. The large quartz grains, the high porosity, and the sparsity of the calcite matrix of the sandstone of sample AR-J result in a high topography where varnish only fills up the interspaces (Fig. B-(C) in the appendix). Material might be washed into these areas and larger dust grains can become caught without the potential to be blown away after leaching. This varnish does not cover the whole surface, and quartz minerals stick out (Fig. B-(B) in the appendix). This is dissimilar to the sample AR-Y, which is fully covered by varnish (Fig. B-(C) in the appendix). Both sandstone host rocks have a $CaCO_3$-rich cement. However, according to polarization microscopy (Fig. B-(E, F) in the appendix), the sandstone AR-Y has much smaller quartz grains than AR-J, and therefore no similarly steep topography can arise. Furthermore, the sandstone AR-J has a larger percentage of pore volume, and the matrix material is rare. The large minerals, the pore space, and the sparsity of the matrix material result in a brittle cohesion of sample AR-J, due to the high quartz grain/cement ratio, and also in superelevation of the surface topography. The lack of layers is not due to a vertical sample exposure, since similar layering was found covering a non-horizontal sample collected in Yatib (Fig. C and D in the appendix).

4.2 Major and trace element determination by fs LA-ICP-MS

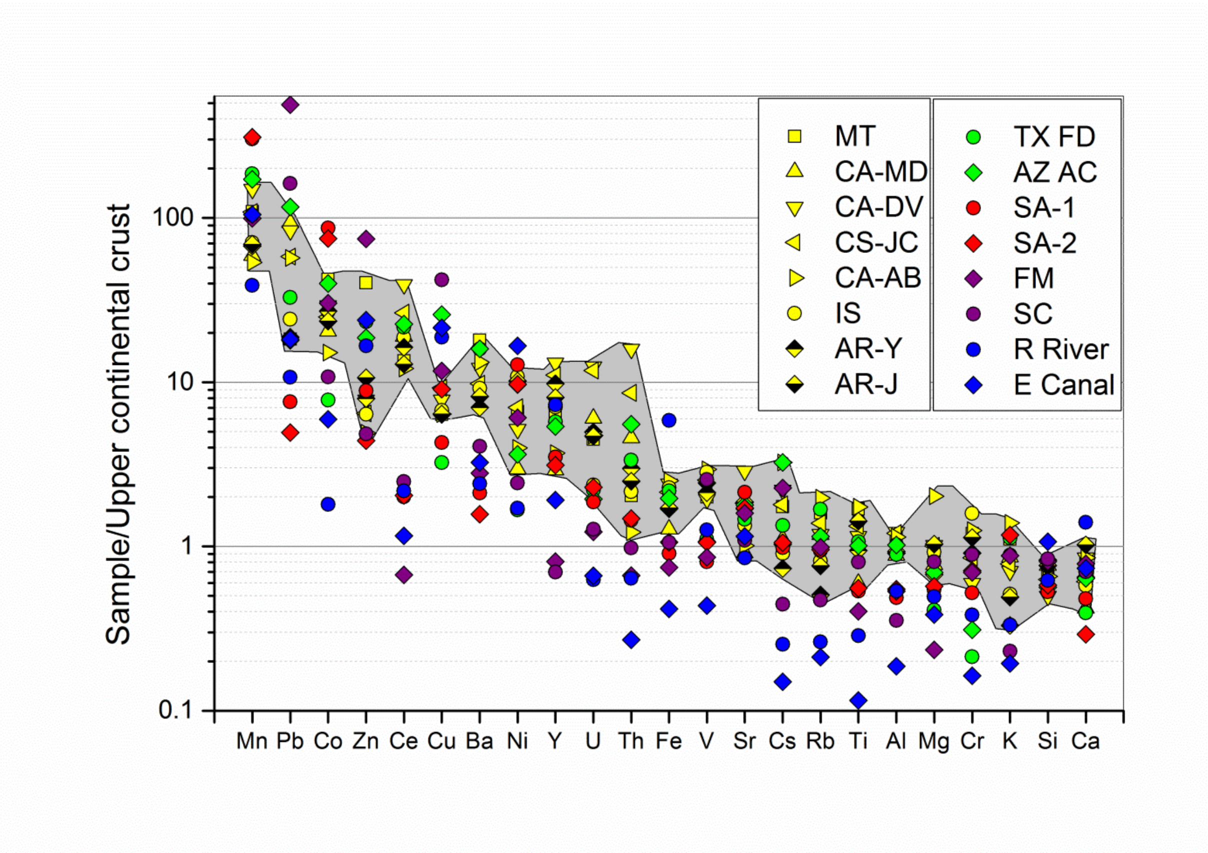

Figure 2: Chemical composition of different varnishes from different regions, sorted by their average mass fractions. The gray shaded area is the plotting area of Type I varnish. All Type I varnishes plot within this relatively narrow field, while none of the other varnishes falls within this field for all elements. Only Type II varnish matches Type I varnish for most elements (exceptions are the transition metals Co, Cu, and Cr). Color code: Yellow: Type I varnish; green: Type II varnish; red: Type III varnish; purple: Type IV varnish; blue: Type V varnish.

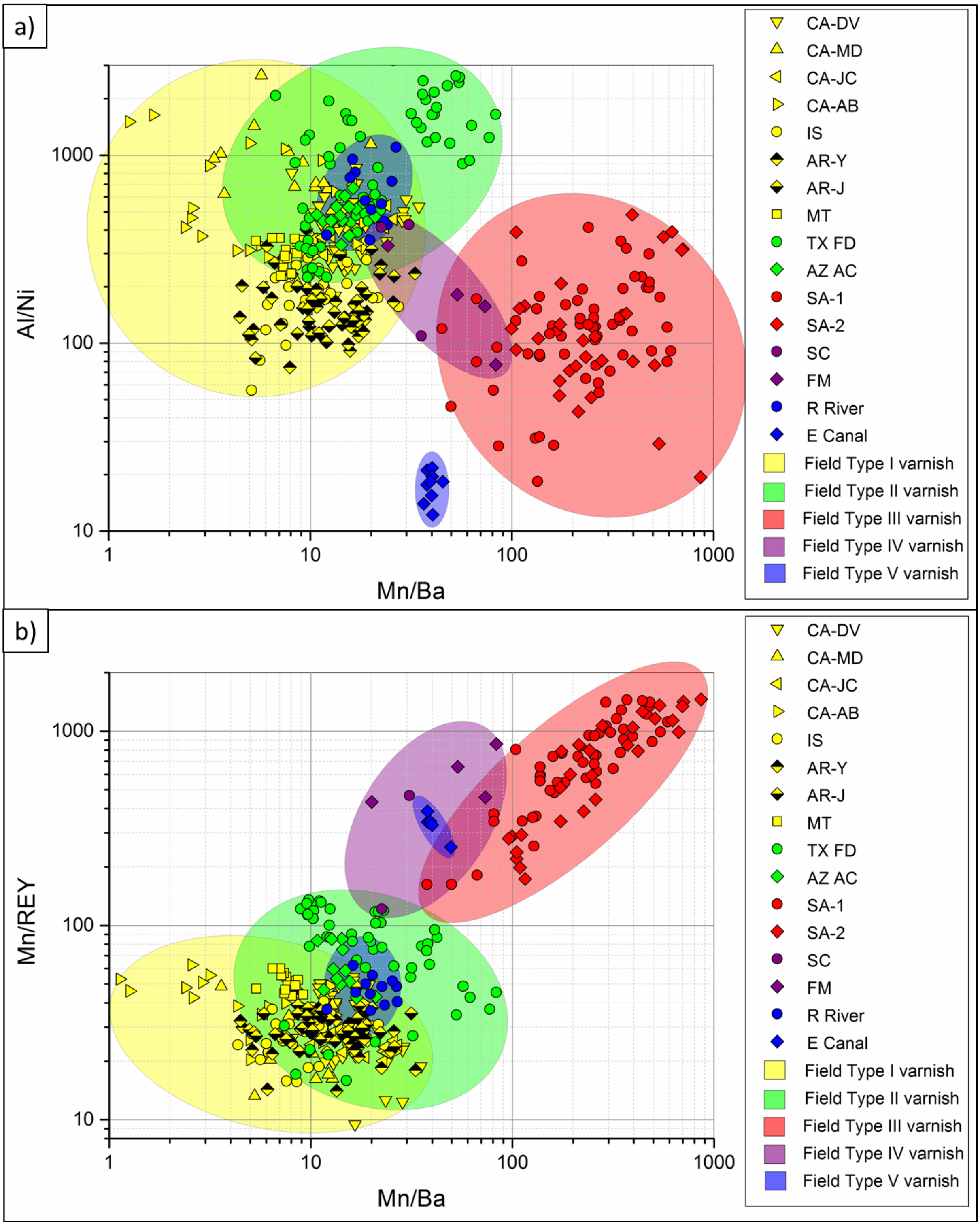

Figure 3: a) Al/Ni vs. Mn/Ba ratio plot and b) Mn/REY vs. Mn/Ba ratio plot for all measured varnish samples. Fields, in which one type of varnish plots, are colored in the corresponding color codes. Type I, and III varnishes plot significantly apart from each other. The Type II varnish field overlaps with the Type I varnish field. Type V varnish plots in two different fields for samples from two different rivers. This indicates that river water is the main element source for Type V varnish. Type IV varnish intercepts Type II, III, and V varnish fields. Color code: Yellow: Type I varnish; green: Type II varnish; red: Type III varnish; purple: Type IV varnish; blue: Type V varnish.

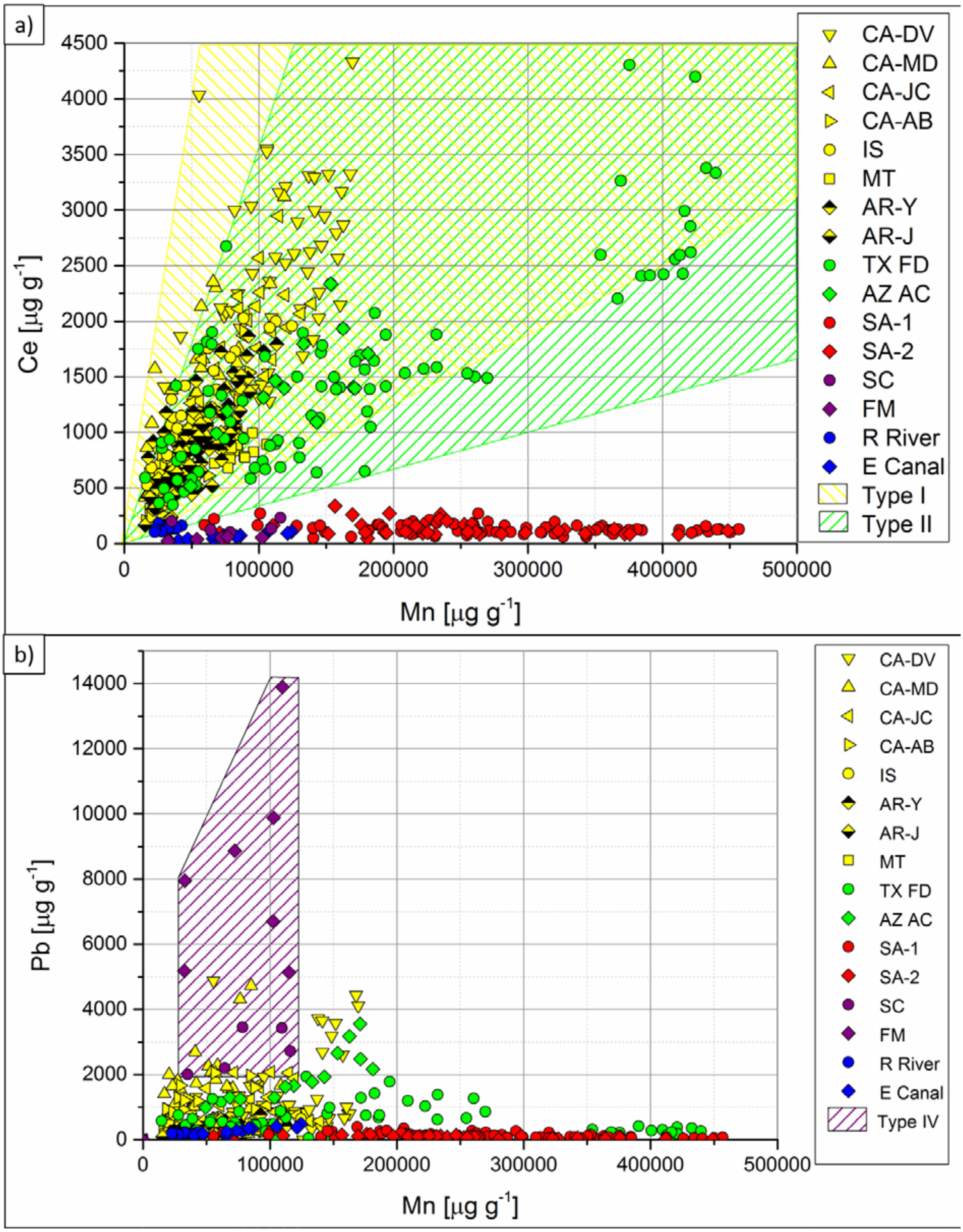

Figure 4: a) Ce vs. Mn plot for all measured varnish samples. A significant correlation between Mn and Ce is only observable for all Type I and II varnishes. All other varnishes show no significant correlation. b) Pb vs. Mn plot for all measured varnish samples. Only Type IV varnish shows a significant enrichment of Pb, independent of the Mn mass fraction, of 0.2-1.4% Pb. Color code: Yellow: Type I varnish; green: Type II varnish; red: Type III varnish; purple: Type IV varnish; blue: Type V varnish.

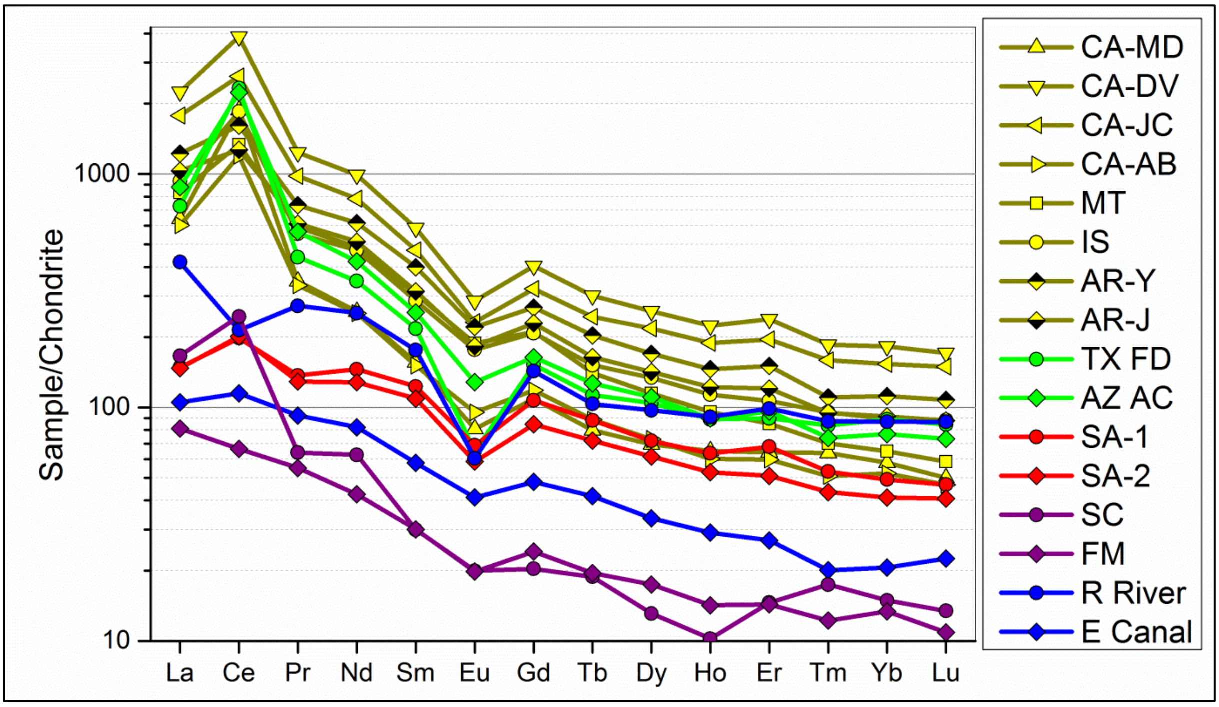

Figure 5: Rare earth element patterns normalized to a chondritic composition (Evensen et al., 1978). All Type I, II, and III varnishes show a positive Ce anomaly. All Type I and II varnishes show a significant enrichment of light REEs (LREEs) relative to heavy REEs (HREEs). Type V and IV varnish show all the possibilities: positive, negative, and no Ce enrichment. Color code: Yellow: Type I varnish; green: Type II varnish; red: Type III varnish; purple: Type IV varnish; blue: Type V varnish.

Femtosecond LA-ICP-MS is a reliable tool to measure major- and trace element concentrations. In this work, 39 element mass fractions were measured for each rock varnish. From each sampling site, one to nine varnish samples were investigated, depending on the sample material available, and on each sample nine to fifteen micro-basins were analyzed to obtain average element compositions. To allow a better overview, Fig. 2 shows the range in which the typical arid desert varnish samples plot as a gray shaded field. Only Type I varnish plots within this range for the elements analyzed. However, Type II varnishes only diverge for the transition metals Cu, Co, and Cr. The other varnish types differ from this field with regard to several elements. Some element mass fractions, such as for Ce, are even more than ten times lower for some varnishes. Concerning Ba, none of the rock varnishes besides Type I and II plot within the gray-shaded range. This is also expressed in Fig. 3, showing that most Type I varnish measurements plot on the x-axis (Mn/Ba) at lower values than the majority of the other varnishes. Our results show that different rock varnish types can be separated from each other based on their chemical composition (Figs. 2-5), only Type I and II varnishes are not easily distinguishable by their chemical composition.

Of the rock varnishes plotted in Fig. 2, only Type II varnish has equally high Ce mass fractions as Type I. This can be explained with Fig. 4 a), where Mn is plotted versus Ce. A clear positive correlation between Mn and Ce can be observed for all Type I and II varnishes. However, the correlation is less pronounced and scatters considerably for the latter. All other rock varnishes (Type III, IV, and V) show no significant correlation between the mass fractions of Mn and Ce, and are generally low in Ce. Of all rock varnishes, only Type IV shows extremely high Pb concentrations (0.2-1.4%; Fig. 4 b), which is not unexpected considering their urban origin. No correlation between the Mn amount and the Pb mass fraction can be observed.

Figure 5 shows an REE plot for all rock varnish types. A clear discrimination can be made between Type I and II varnish and the other rock varnishes by the combination of Ce enrichment (arid: Ce/Ce*=1.5-3.8), enrichment in light REE (arid: La_N/Yb_N= 10.4-12.9), the negative Eu anomaly (arid: Eu/Eu*= 0.6-0.7), and the overall REE mass fraction (arid: 3200-11200 µg g^{-1}).

Additionally, dust collected adjacent to varnish was investigated, since this dust is thought to be the major source for the enriched elements. Detailed studies on the dust component are to be published by Otter (in preparation). The REE patterns (Fig. E in the appendix) show that Type I varnish is strongly enriched compared to the adjacent, fine grained dust, even though the fine grained dust is already more than two times enriched compared to the coarse grained (> 50 µm) dust (Otter, in preparation). The dust does not show a positive Ce anomaly, but the La_N/Yb_N ratio is similar for all dust samples, and similar to that of the varnishes. There is almost no REE enrichment in varnish SA-2 compared to the adjacent dust, but a small positive Ce anomaly can still be observed in the former.

Comparing varnish and dust ratios shows that a fractionation factor exists, which is identical for all Type I varnishes. It matches the fine fraction (<50 µm) of arid desert mineral dust to the associated rock varnish (Fig. F in the appendix). This factor is 9 for the Mn/Ba ratio and 0.2 for the Al/Ni ratio. It is not possible to match all coarse-grained arid desert dusts to the corresponding rock varnishes using the same factor for all samples. This is not surprising, since it is likely that only the fine-grained particles are responsible for the varnish accumulation. However, mineral dust from the semi-arid desert cannot be matched to the corresponding Type III varnish using the same factor. To match the fine fraction to the varnish for this rock varnish type, a factor of about 16 for the Mn/Ba ratio and 0.06 for the Al/Ni ratio is needed.

4.3 Matrix material investigations by electron paramagnetic resonance spectroscopy

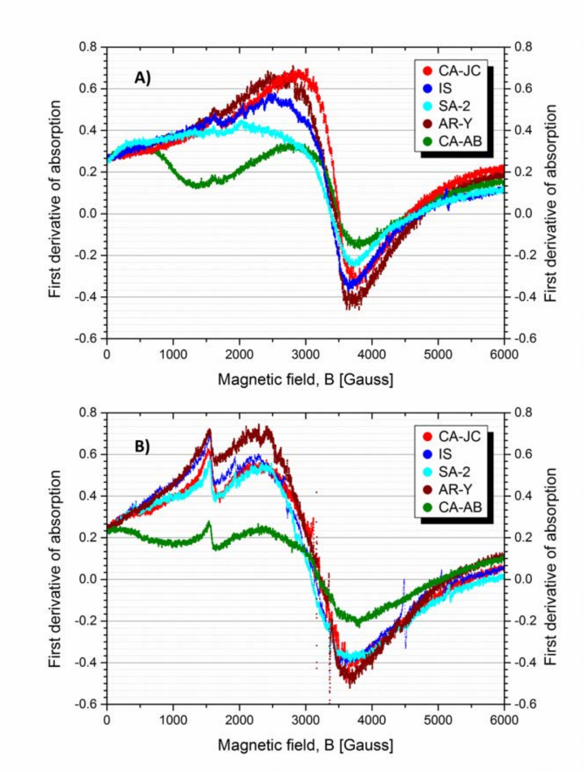

Figure 6: Electron paramagnetic resonance spectra of five rock varnish samples (SA10 #9a, CA14 JC1, IS13 V2, AR14 Y1, CA13 AB2-2). A) spectra measured at RT (about 293 K) and with 0.23 mW. B) spectra measured at 90 K and with 0.22 mW. In all spectra, a Fe^{3+} peak can be observed at about 1500 G on the flank of the relatively narrow (560-1200 G) Mn absorption peak.

We investigated rock varnishes of Type I and III from five locations (SA10 #9a, CA14 JC1, IS13 V2, AR14 Y1, CA13 AB2-2; Fig. 6) and compared the results to EPR measurements from a Type IV varnish from the Smithsonian Castle measured and published recently (Livingston et al., 2016). Figure 6 shows RT and 90 K measurements at low (0.22-0.23 mW) power settings. Spectra at high power setting (209-225 mW) are plotted in Fig. G of the appendix. All samples show similar resonance peaks. They exhibit the Fe^{3+} resonance at about 1500 G, which became more pronounced at lower temperatures. The typical peak related to Mn oxyhydroxide appears at about 3300G. The broad linewith of the signal can be attributed to the spin-spin interaction due to the high concentrations of paramagnetic centers in local domains that give rise to a strong exchange interaction, as described by Kim et al. (2011). The signal was slightly broader for lower temperature (90 K) measurements, indicating the absence of Mn^{2+}-Mn^{2+} isolated pairs (Kim et al., 2011). The fine six-line patterns due to highly dispersed Mn^{2+} at low concentrations (Kim et al., 2011) appeared in the low-power spectra of the IS, CA-AB, CA-JC, and SA-2 samples at 90 K on the main resonance peak flank (Fig. 6 B). The measured spectra resemble the spectrum of the Type IV rock varnish presented by Livingston et al. (2016) and measured at 77 K, 10 mW, and 9.38 GHz, close to the settings for the spectra plotted in Fig. 6 B.

All samples fall into the category of intermediate linewidths (about 800-1100 Gauss) and are therefore indicators for an aged Mn bio-oxide. However, there are several differences between them. Sample CA-AB shows an initial rise of the signal, similar to that of all other samples, followed by a strong decline with increasing magnetic field. Also sample SA-2 shows a much broader peak shoulder and a lower peak amplitude at RT than the samples IS and CA. This pattern changes with decreasing temperature settings, resulting in a similar spectrum at 90 K, compared to the other samples. These phenomena could be attributed to the presence of domains with ferrimagnetic or antiferromagnetic properties that induce a complex behavior in response to the application of an external magnetic field and to the temperature change.

4.4 Element distribution maps by scanning transmission X-ray microscopy

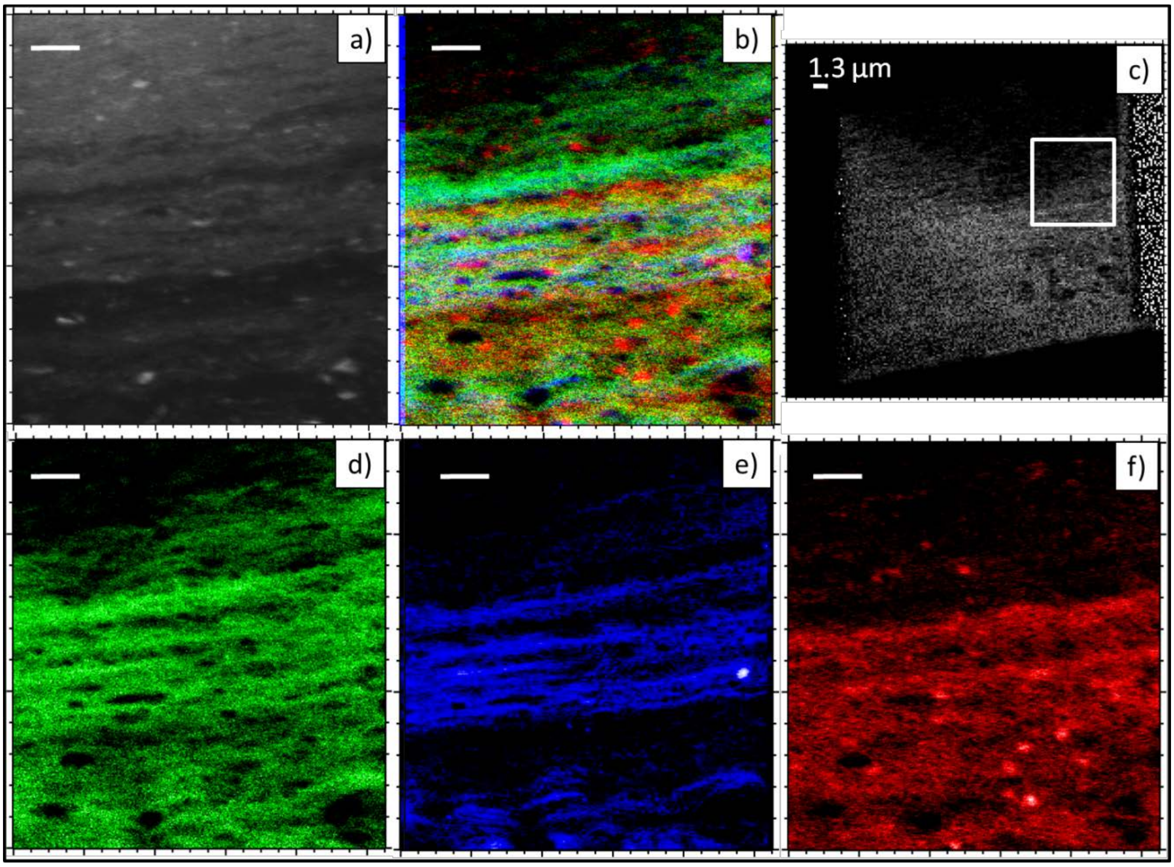

Figure 7: Element distribution maps obtained by scanning transmission X-ray microscopy. Maps and images of Type I varnish, sample CA14 JC-8. Scale bar represents 1.3 µm, image a) was taken at 293 eV, b) is an overlay of Fe (red), Mn (green), and Ca (blue), c) is an overview image, d) a Mn map, e) a Ca map, and f) a Fe map.

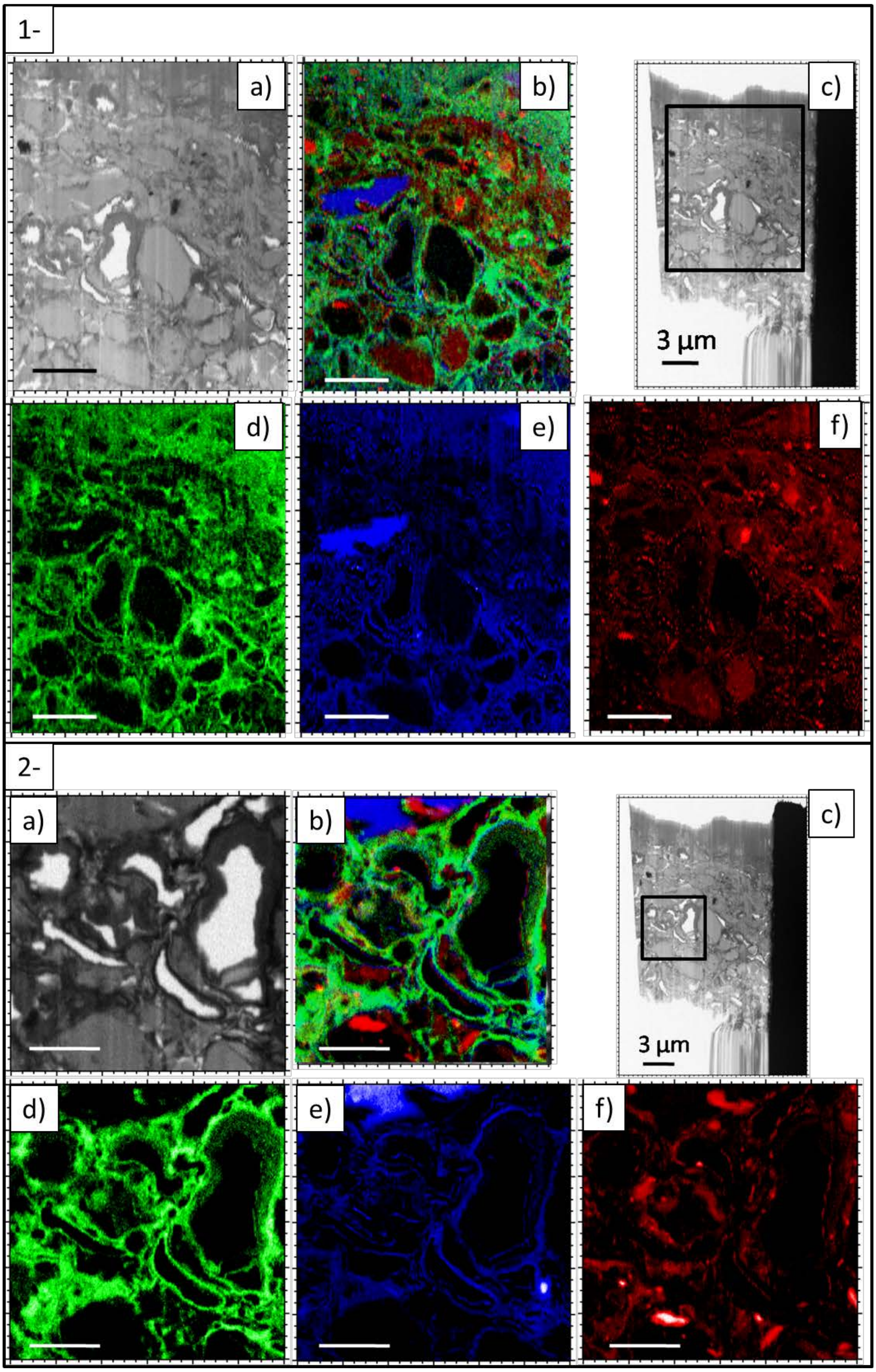

Figure 8: Element distribution maps obtained by scanning transmission X-ray microscopy. Maps and images of Type II varnish. All images were obtained from sample TX FD 1. Scale bar represents 3 µm, Fig. 8-1 are overview images, Fig. 8-2 are close-up maps. Image a) of Fig. 8-1 was taken at 530.5 eV, b) is an overlay of Fe (red), Mn (green), and Ca (blue), c) is an overview image, d) a Mn map, e) a Ca map, and f) a Fe map. Image a) of Fig. 8-2 was taken at 642 eV, b) is an overlay of Fe (red), Mn (green), and Ca (blue), c) is an overview image, d) a Mn map, e) a Ca map, and f) a Fe map.

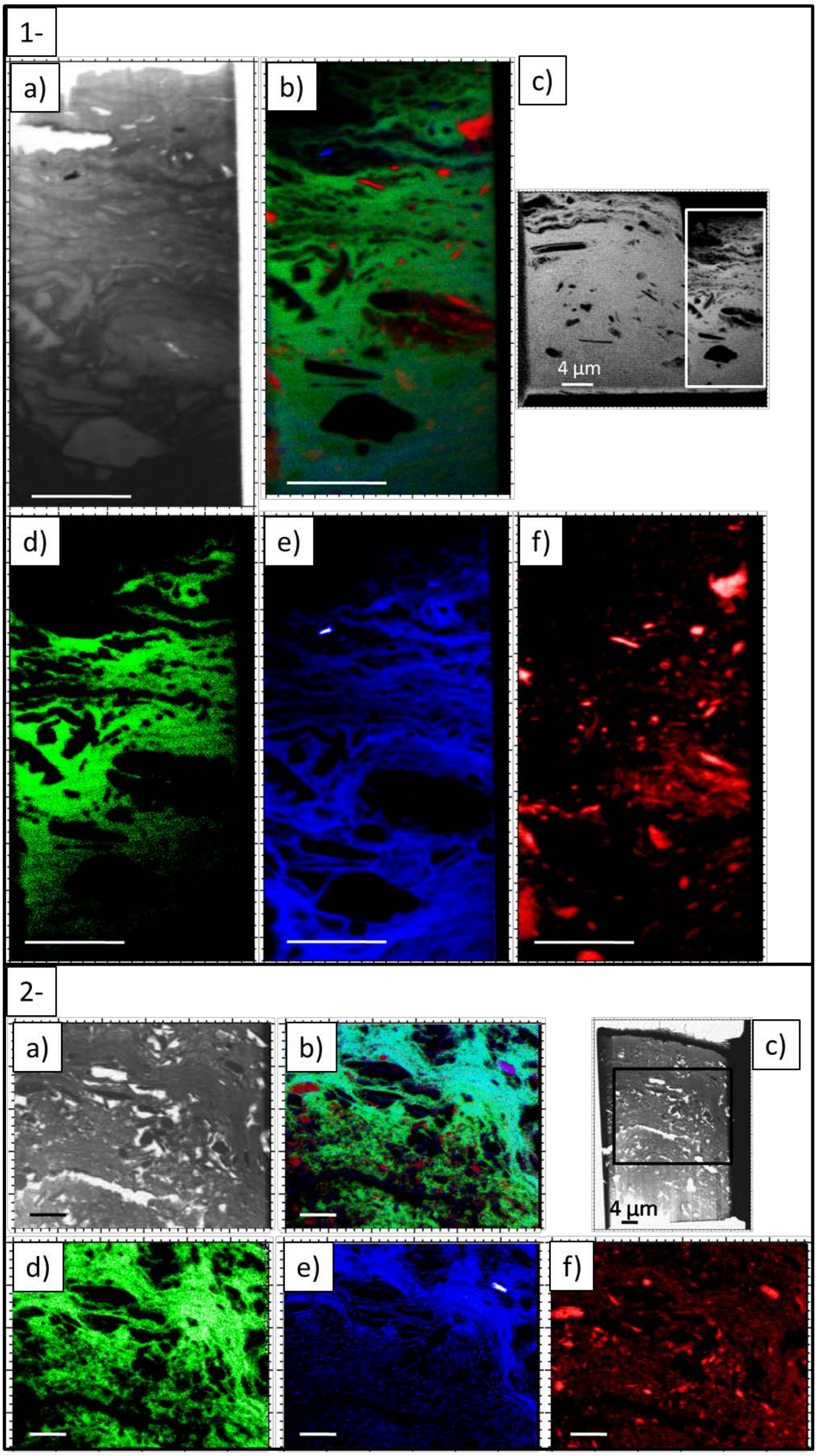

Figure 9: Element distribution maps obtained by scanning transmission X-ray microscopy. Maps and images of Type III varnishes. Images of Fig. 9-1 show sample SA 14 09a, images of Figure 9-2 sample SA13 mM-f. Figure 9-1: Scale bar represents 4 µm, image a) was taken at 349 eV, b) is an overlay of Fe (red), Mn (green), and Ca (blue), c) is an overview image, d) a Mn map, e) a Ca map, and f) a Fe map. Figure 9-2: Scale bar represents 4 µm, image a) was taken at 342 eV, b) is an overlay of Fe (red), Mn (green), and Ca (blue), c) is an overview image, d) a Mn map, e) a Ca map, and f) a Fe map.

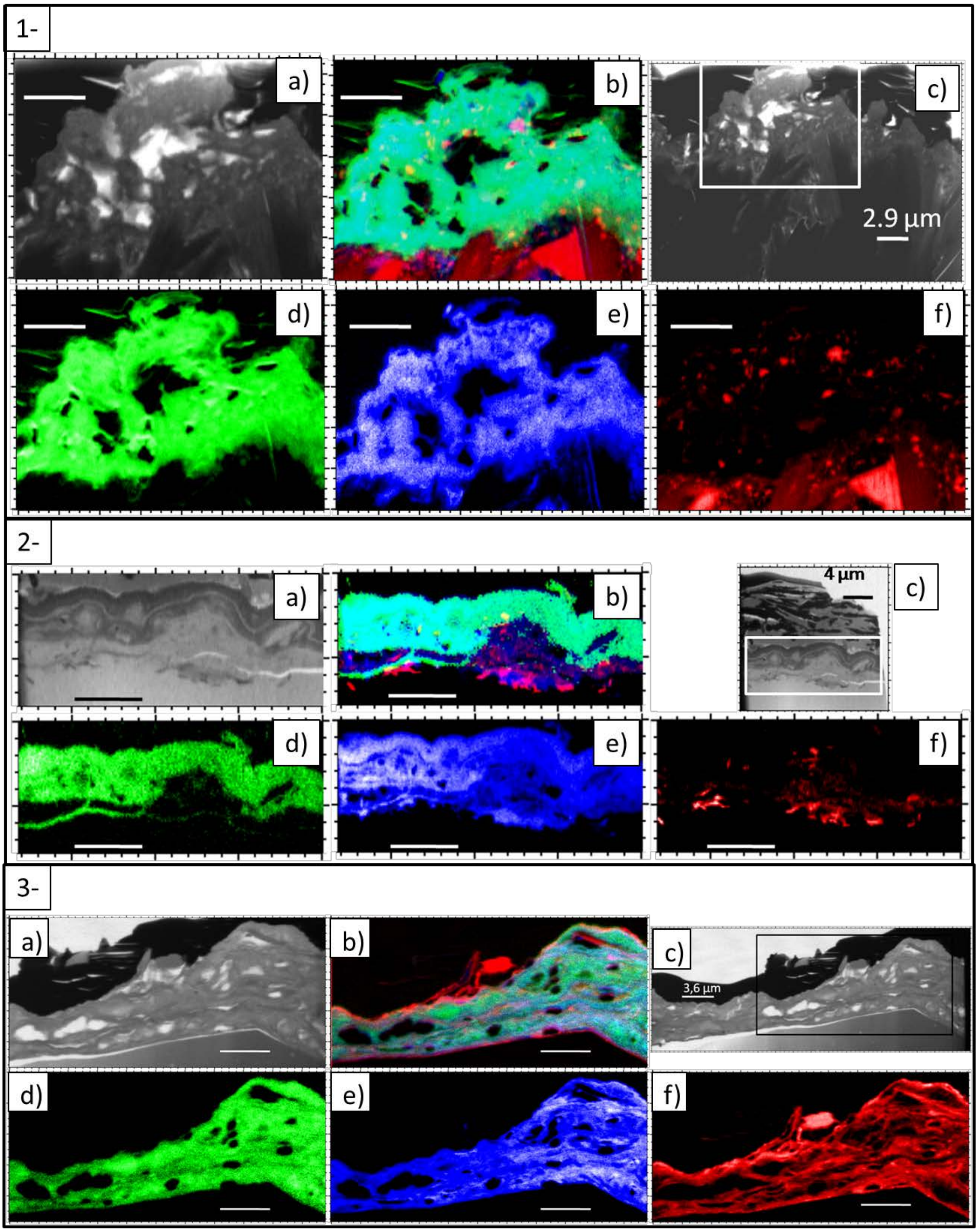

Figure 10: Element distribution maps obtained by scanning transmission X-ray microscopy. Images and maps of Type IV and V varnishes. Images of Fig. 10-1 show sample SC (Type IV), images of Figure 10-2 sample FM (Type IV), images of Fig. 10-3 show sample E Canal (Type V). Figure 10-1: Scale bar represents 2.9 µm, image a) was taken at 637 eV, b) is an overlay of Fe (red), Mn (green), and Ca (blue), c) is an overview image, d) a Mn map, e) a Ca map, and f) a Fe map. Figure 10-2: Scale bar represents 4 µm, image a) was taken at 530.5 eV, b) is an overlay of Fe (red), Mn (green), and Ca (blue), c) is an overview image, d) a Mn map, e) a Ca map, and f) a Fe map. Figure 10-3: Scale bar represents 3.6 µm, image a) was taken at 525 eV, b) is an overlay of Fe (red), Mn (green), and Ca (blue), c) is an overview image, d) a Mn map, e) a Ca map, and f) a Fe map.

The element distribution maps at the nm scale were obtained by STXM-NEXAFS. These measurements were additionally used for oxidation state determinations ($Fe^{2+/3+}$, $Mn^{2+/3+/4+}$), and for the determination of functional groups and moieties of carbon. In this work, only STXM-NEXAFS maps of Mn, Fe, and Ca are shown, emphasizing the presence or absence of layered structures in varnishes from different environments. Figures 7, 8, 9 and 10 show the different varnish types. Only the typical Type I varnish sample reveals continuous and horizontal Mn-, Fe-, and Ca-rich layers. Calcium occurring together with Mn in rock varnish was previously described by Raymond et al. (1993), an observation which can be confirmed by our data. Calcium often shows sharper features in all varnishes than Mn. In contrast to Mn, Ca and Fe are also present at higher amounts in mineral dust particles. While Type I, III, and V varnishes show Fe-rich layers, Type II and IV varnishes show only Fe-rich minerals and areas instead of layers. Type III varnish can be subdivided into two appearance groups: a) dense, homogenous varnish without cavities (Fig. 9-1), and b) cavity-rich varnish, which shows some botryoidal, cauliflower-like Mn-sheets, interspersed by areas containing nests of larger mineral particles (Fig. 9-2). Type II varnish shows areas that are Fe-rich and Mn-poor, but no layering is observable. Large, rounded mineral grains and elongated clay minerals are integrated into the varnish matrix (Fig. 8-1). Manganese and Ca are especially enriched at the mineral grain-matrix contacts and along the rims of cavities (Fig. 8-2). Type IV varnish FM (Fig. 10-2) shows Fe-rich particles almost only at the host rock - varnish boundary; they might therefore have acted as nucleation particles for Mn oxyhydroxide mineral growth (Burns and Brown, 1972).

5. Discussion

5.1 Element distribution, element composition, absorption properties, and structures

Dust contribution

Our results show that the chemistry of different rock varnishes is quite diverse. However, the element composition of Type I varnish does not vary significantly among the worldwide sampling locations. The similar element mass fractions might be interpreted as the result of dust sources of similar element compositions. However, this would be surprising, given that the samples were collected on several different continents with presumably different dust compositions. On the other hand, the widely differing plotting clusters for the different rock varnish types cannot be explained only by varying dust compositions, since these show much smaller differences, as shown in Fig. F in the appendix. It is rather probable that different formation processes are responsible or different Mn oxyhydroxides are present.

Ba, Ni, and Pb

A likely explanation for the observed similarities and dissimilarities are the existence of similar or different Mn oxyhydroxide crystal structures or growth conditions, such as the pH ranges. For Mn oxyhydroxides with different crystallographic structures, surface chemical properties, such as the adsorption and desorption capacity of heavy metals, differ significantly from each other (Feng et al., 2007; Li et al., 2004; Pan et al., 2004). This can result in the preferred sorption of certain positively charged elements such as e.g., Ni^{2+} or Ba^{2+}. These two elements are of particular interest, since their incorporation into Mn oxyhydroxides is different. While Ba is a large ion (diameter Ba^{2+} ~ 2.5 Å) that can only occupy large vacant positions, such as intra-tunnel sites, the transition metal, Ni (diameter Ni^{2+} ~ 1.49 Å), can be incorporated in tunnels, between sheets, or even as substitute for Mn (diameter $Mn^{2+/4+}$ ~ 1.6/1.4 Å).

Large atoms, such as Ba and Pb, are thought to destroy sheet structures and stabilize or promote tunnel structures (Tebo et al., 2004). However, some authors claim that the Mn oxides in desert varnish commonly resemble poorly crystalline birnessite (Potter and Rossman, 1979), a sheet structure mineral which is often of biogenic origin. The high amount of large cations observed in arid desert varnish is in conflict with the presumption of pure birnessite as prevalent Mn oxyhydroxide phase, and indicates that either partially aged and transformed (e.g., sheet structure to tunnel structure) minerals such as hollandite ($Ba_x(Mn^{4+}, Mn^{3+})_8O_{16}$) are abundant, which is also in agreement with our EPR investigations, or that an initial mixture of birnessite with other tunnel Mn oxides existed, as stated by McKeown and Post (2001). Figure 5 shows that only in Type I and II varnishes the Ba mass fraction is strongly enriched, while the enrichment for Pb, also a large cation (diameter Pb^{2+} ~ 2.4 Å), is highest in Type IV varnishes (Fig. 4 b). A reason for this behavior might be the differences in Pb availability in the surrounding environment, since Pb is highly abundant in urban areas and along roadsides (Lytle et al., 1995), as reflected in the high enrichment in the urban varnishes (Figs. 2 and 4b).

Further factors accounting for the large differences between Pb enrichments of different varnish types might be different pH conditions or ligand abundances. Lead can be bound as hydroxy complex on the external basic surfaces of clay minerals (Rybicka et al., 1995) or Mn oxyhydroxides (Feng et al., 2007). It competes with H^+ ions with decreasing pH, since H^+ can rapidly exchange the Pb ion (Rybicka et al., 1995). Since Pb has a large ionic diameter (2.4 Å), it has a lower charge density and is more affected by the protonation than other transition metals, such as Ni (Abollino et al., 2003). Lead also forms more stable and larger complexes in the presence of ligands with longer hydrocarbon chains. This decreases the adsorption potential, since the complexes are too large to be introduced into interlayer sites (Abollino et al., 2003).

Trace element enrichment behavior

As shown in Fig. 2, many cations, such as Pb, Co, Ce, Ba, Y, Ni, U, Th, Fe, and Sr, are highly enriched in rock varnish. Figure 2 also shows that the Type I and II varnishes have much higher adsorption potentials than the other varnishes. The different adsorption behavior might be an indicator for another mode of origin, since e.g., biogenic and non-biogenic Mn oxides differ in their sorption behavior. Bio-oxides have structurally less Mn^{3+}, since they are generated by two one-electron transfers from Mn^{2+} over Mn^{3+} to Mn^{4+}, where Mn^{3+} is a non-solid intermediate and exists only in solution (Tebo et al., 2004). Available Mn^{3+} will be generated secondarily when the Mn oxyhydroxide functions as electron acceptor, i.e., as oxidant. The sorption of Mn bio-oxides occurs primarily at vacancies, which are common in the usually poorly crystalline Mn bio-oxides, or on biofilms or bacterial sheaths, which are produced by the organisms during the precipitation (Tebo et al., 2004). Furthermore, biogenic oxides are usually actively growing in the presence of contaminant metal ions (Tebo et al., 2004) and therefore the cation enrichment is often higher in bio-oxides than in abiogenic Mn oxyhydroxides. However, the clay mineral fraction in rock varnish, deposited and incorporated earlier, might also contribute to the element sorption of, e.g., Pb, Cd, Cu, Ni, and Zn (Rybicka et al., 1995). Type II varnish element enrichments are very similar to those of Type I varnishes. The exceptions, Co, Cu, and Cr, might be results of either different growth mechanisms, or sources with different transition metal contents.

Rare earth elements

The high positive Ce anomaly shown in Fig. 5 might be an indicator for the growth rate of the varnishes (Bau et al., 2014). Cerium, dissimilar to the other REEs whose highest oxidation state is REE^{+3}, is the only REE that can also exist at a higher positive valence state (Ce^{4+}). Manganese oxides are one of the strongest naturally occurring oxidants and participate in a wide range of redox reactions. Manganese oxyhydroxides can function as electron acceptors for the oxidation of Ce:

$Ce^{3+}_{(aq)} + MnO_{2(c)} + 2H_2O_{(l)} = CeO_{2(c)} + MnO(OH)_{(c)} + 3H^+_{(aq)}$ (Ohta and Kawabe, 2001)

or

$2Ce^{3+}_{(aq)} + MnO_{2(c)} + 2H_2O_{(l)} = 2CeO_{2(c)} + Mn^{2+}_{(aq)} + 4H^+_{(aq)}$ (Ohta and Kawabe, 2001)

By this process, the Mn oxyhydroxide gains additional negative charge, which can be balanced by further adsorption of cations. The generated Ce^{4+} can precipitate as insoluble cerium dioxide (CeO_2), explaining the enrichment of Ce compared to the other REEs, which are only enriched by the process of sorption, where they are in competition with other ions.

The plot Ce vs. Mn (Fig. 4 a) shows the increase of Ce for different Mn mass fractions for Type I and II varnish. The faster the varnish grows, the less Ce can be precipitated on the uppermost layer, since the Ce accumulation is depending on the availability over a certain time period (Bau et al., 2014). Figure 4 a) thus indicates a higher growth rate for most of the Type II varnishes compared to Type I varnish. Furthermore, while Type I varnishes are highly enriched in REEs relative to their dust sources, Type III varnishes seem to have only a very low enrichment in comparison to the adjacent mineral dust (Fig. F in the appendix). This observation is in agreement with the lack of an increase of Ce for higher Mn mass fractions (Fig. 4 a).

Al/Ni vs Mn/Ba ratios

Since Al is distributed fairly homogeneously in rock varnish (Goldsmith et al., 2014) and Ba occurs together with Mn (Raymond et al., 1993), we chose a plot of the Al/Ni vs the Mn/Ba ratios for a comparison of the different varnish types (Fig. 3 a). Additionally we chose Mn/REY vs. Mn/Ba since we can express the enrichment of the elements Ba and the REY independent of the Mn mass fractions (Fig. 3 b). All these elements are mainly enriched within the Mn-rich phase. Figure 3 shows that the varnishes from similar environments plot together in discrete fields, distinguishing the various varnish types. Only the two Type V varnish samples plot apart from one another, even though they were collected from a similar environment (river splash) and from locations not far apart. This can be explained if their primary ion source is river water with significantly differing ion abundances, and not mineral dust with a composition close to the UCC. The cation availability is presumably different for the large natural Adirondack River and the small man-made Erie Canal. The Type I and III varnishes plot in well-separated fields, while Type IV varnish intercepts other varnish fields. It can be separated by its Pb content (Fig. 4 b). Type I and II varnish cannot be clearly separated by this plot, even though they differ in their features, such as layering, stromatolitic features, and crust thickness.

Manganese-rich mineral matrix

To investigate the role of the crystal structures of the Mn oxyhydroxides in the matrix material of Type I and III varnish, we studied EPR spectra of several rock varnish samples. The spectra were also compared to a spectrum of sample SC (Livingston et al., 2016) , a Type IV varnish and they were all considered in the context of the biogenic-abiogenic plot published by Kim et al. (2011). We found that all investigated samples fall within the range of materials formed originally as Mn bio-oxides, based on the interpretation by Kim et al. (2011). Beyond this overall finding, we observed some differences between samples. The varnishes investigated can be subdivided into three categories: Type I varnish samples CA-JC, IS, and AR-Y show an EPR pattern similar to that of sample SC, which is a Type IV varnish. One Type I varnish, sample CA-AB, shows a lower absorption peak. It is unclear if this is the result of a different composition and mineralogy, or if other factors are involved, such as more host rock material within the varnish powder, due to the abrasion during the sample preparation. Type III varnish reveals a significantly different absorption peak shape, comparing high and low T absorption (Fig. 6). This is typical for a saturated sample. It is therefore conceivable, that this sample has a higher abundance of layer site vacancies, and therefore a lower number of close neighbors, which suggests an even higher probability for a biogenic origin of this sample, or a more recent genesis with less time for transformation processes. This observation is also true, but less distinct, for sample CA-AB, a Type I varnish.

Manganese and iron layering

The observations by STXM-NEXAFS give new insights into the application of rock varnish as local paleoclimate archive. The absence of parallel continuous layers of Fe and

Mn in varnishes other than Type I exclude them from becoming a paleoclimate archive using the established method of Mn and Fe layer correlation (Dorn, 1984). This paleoclimate reconstruction technique is based on the assumption that Mn-rich layers represent wet climates and Fe-rich layers dry climates (Broecker and Liu, 2001).

The reason for the lack of layers in the arid desert varnish sample AR-J is most probably the loose, $CaCO_3$-rich cement of the underlying rock in combination with the relatively large quartz grains. These prevent a fully closed varnish coating due to superelevation of the topography and may also cause further movement, disordering, and rearrangement of possibly former existing layers. Therefore, the full cover of the host rock by varnish, as well as the type of underlying rock, have to be considered when one searches for possible paleoclimate archives.

Calcium

In all rock varnishes investigated, Ca occurs together with Mn, probably due to the ability of Mn oxyhydroxides to adsorb and incorporate Ca. This was suggested by Raymond et al. (1993), who came to this conclusion on the basis of a positive correlation between Mn and Ca in their bulk varnish samples. Our microanalytical techniques allowed us to demonstrate this relationship more specifically by showing a high abundance of Mn and Ca at the same sites within the samples. The STXM-NEXAFS element maps proved that Ca and Mn are distributed similarly in the varnish, and that Ca is incorporated into the Mn-rich matrix and not as separate mineral phases. Calcium can be adsorbed into inter-tunnel and inter-sheet sites, it can replace Mn in octahedral sites, or fill vacant octahedral sites in Mn oxyhydroxides. Therefore, in addition to the option of applying Mn/Fe and Ba/Fe as paleoclimate proxies, Ca/Fe layering within Type I varnishes might be suitable as well, since the Ca-layers seem to be more pronounced than the Mn-layers, based on the STXM-NEXAFS observations in this work (Fig. 7, 8, 9, and 10).

Stromatolitic features

Manganese stromatolites were described from a cave in Spain by Lozano and Rossi (2012) and Rossi et al. (2010). A commonality of some of the varnishes investigated here with these cave Mn stromatolites are the structures observed, such as dendritic layers that branch upward and outward (Rossi et al., 2010). This description is especially applicable to Fig. 1 F, and was also observed in Type II varnish. However, the stromatolites described by these authors had dimensions in the cm range, with lamination thicknesses of 1-5 µm (Rossi et al., 2010), while in our samples the structures have an overall thickness of only a few micrometers.

5.2 Different types of rock varnish

Based on microanalytical studies, our study shows that the term “rock varnish” requires classification into further types, related to their formation environment, microstructure, and chemical composition. We propose to subdivide rock varnish into the following types:

Type I varnish

Type I varnish can be found in arid deserts and shows fine-grained laminated structures (Fig. 1 A, B), with small (1-10 nm) mineral dust particles. Superelevated structures within the host rock surface hamper the formation of layers (Fig. 1 E). Alternating Mn- and Fe-rich layers, continuous and parallel to the host rock surface, might reflect paleoclimate fluctuations. These layers were only clearly observable in Type I varnish (Fig. 7). The thickest varnish and best layerings are observable in microbasins, i.e., small depressions on horizontal rock surfaces. Next to Mn-rich layers, a second layering can be observed, which seems to be a result from varying amounts of mineral grains, with different element compositions. These layers are probably representing different dust fluxes and sources. Type I varnish has a distinct element composition of high REEs (Ce/Ce*=1.5-3.8, La_N/Yb_N= 10.4-12.9, Eu/Eu*= 0.6-0.7, total REE mass fraction 3200-11200 µg g^{-1}) and high Ba mass fractions. Cerium mass fractions are positively correlated with Mn mass fractions (Fig. 4 a), and all samples show a positive Ce anomaly (Fig. 5). Type I varnish shows EPR spectra that indicate an originally biological genesis which aged and transformed with time (Fig. 6). The varnish coating is highly enriched in REEs compared to mineral dust collected nearby (Fig. E, appendix).

Type II varnish

Type II varnishes, collected in semi-arid deserts, have larger Fe-rich areas and large, rounded mineral particles (Fig. 1 I). They often show upwards and outwards branching structures on the µm scale within the profile, and no Mn layering is detectable at the 100 nm to µm scale. The surfaces of these varnishes often reveal nodules grown on top of the exceptionally thick crusts (up to 500 µm thick Mn-rich crusts). Manganese, Fe, and Ca form rims around grains and cavities (Fig. 8-2). Rims lining cavities might be an evidence for either mineralization from a fluid, or precipitation around a former feature, such as a microbial cell. The element composition of Type II varnish is close to that of Type I varnish (Fig. 2), however, divergent for some elements, such as Co, Cu, and Cr. A positive correlation is abundant between Ce and Mn (Fig. 4 a), Ce is highly enriched (Fig. 2), and a positive Ce anomaly was found in all samples (Fig. 5). The Ce vs Mn plot scatters more than that of Type I varnish, and the Ce enrichment is lower for many samples. This indicates a higher growth rate for Type II varnishes than for Type I varnishes. A fast growth is also indicated by the large particles within the matrix (Fig. 1 I). The observation, that the mass fractions of Type II varnish scatter significantly more than those within the Type I varnish group is probably due to the fact that this varnish type grows faster, larger dust particles get incorporated and have a stronger influence on the overall chemical composition of the varnish type.

Type III varnish

Type III varnish, found in a semi-arid desert, shows cavities and large (1-3 µm) angular mineral grains within a Mn-rich matrix (Fig. 1 C, D). Iron is abundant in mineral grains (Fig. 9), in some cases also contributing to the matrix composition, showing features following the botryoidal Mn-layers. Type III varnish shows two distinct internal structures: The first kind of Type III varnish contains large amounts of ellipsoidal cavities within the varnish matrix (Fig. 9-2). Wavy layering of the Mn-rich matrix can be observed, interspersed by chaotic structures with large minerals, mineral grain “nests”, and cavities (Fig. 1 C, D). The second kind has a dense Mn-rich matrix, lacking features such as layers or cavities (Fig. 9-1). These two different kinds of varnish features, both found within one type of varnish, seem to correlate with the sampling site. Structureless, dense varnish coatings were found on pebbles in the middle of varnished patches. They are shiny black in appearance, with a strong metallic luster. The cavity-rich varnishes, showing botryoidal mats of Mn- and Ca-rich material, were collected on pebbles at the rims of those varnished patches. It is likely that the difference in appearance is an aging phenomenon, and the structures change over time. This interpretation is in agreement with the increase of cavities within the matrix from the varnish-rock contact up to the top of the aged varnish crusts (Fig. 9-1). Type III varnish has very high Mn mass fractions (about 40%) and very low Ba and Pb values. It can be distinguished from Type I, II, and V by its Al/Ni vs. Mn/Ba plotting field, and from Type IV by the Pb vs. Mn diagram (Fig. 4 b). The varnish grows from the soil-atmosphere-rock contact upwards and downwards on pebbles, and grows therefore partially subsoil. All samples show a positive Ce anomaly. This varnish has very low enrichment of REEs relative to mineral dust from the adjacent soil, the highest enrichment was observed for Ce (Fig. E, appendix). Based on EPR measurements, an originally biological genesis is indicated for this varnish type, with a more recent formation than for Type I varnish (Fig. 6).

Type IV varnish

Type IV varnish collected from urban building facades shows structures differing from all other varnish types, and differing between two samples within this one type. The two samples investigated seem to have similar fast growth rates (µm per a few decades), environmental surroundings (city areas), and host rock substrates (sandstone). They both appear as patches on building facades. However, the structures observed within ultra-thin sections are dissimilar. Thick, round features were observed in one sample, which are encased by the Mn-rich matrix, resulting in a botryoidal structure (Freiburg Münster (FM), Fig. 1 H). A layering was observed in SEM images of this sample (FM), but the layers are not based on differences in the Mn abundance (Fig. 10-2). A second sample (Smithsonian Castle (SC), Fig. 1 F) showed a structureless matrix with a high abundance of small, angular mineral grains and cavities, and finger-like upwards branching nodes building the upper varnish surface. Type IV varnishes show Fe enrichment only in mineral grains (Figs. 10-1, 10-2). Even though their structures differ significantly, the chemical composition of both samples show very high Pb (0.2-1.4 %) and very low Fe mass fractions. Type IV can be distinguished from Type I and II by the Ce vs. Mn diagram (Fig. 4 a), and from Type III and V by the Pb vs. Mn plot (Fig. 4 b). The samples showed a mixture of positive, absent, and negative Ce anomalies (Fig. 5). This varnish grows quickly, up to about 1 µm per year.

Type V varnish

Type V varnish can be black or dull brown in color. Discontinuous layers of Mn, Fe, and Ca are observable, however, they are not parallel to the rock surface (Fig. 10-3). No major amounts of mineral particles were observed in this type, questioning its belonging to the group of rock varnishes. The element source of Type V varnish is presumably water, based on different plotting fields of samples collected at river sites not far apart (Fig. 3). Due to this source, much lower Th, Cs, Rb, and Ti mass fractions were observed compared to other varnishes. Furthermore, major elements are significantly depleted relative to the UCC (Fig. 2). The samples showed a mixture of positive, absent, and negative Ce anomalies (Fig. 5). Type V varnishes have low Mn mass fractions (3-8 %) and grow rapidly (tens to hundreds of years to thicknesses of about 5 µm) within river splash zones. They can be distinguished from Type I, II, and III varnishes by the Al/Ni vs. Mn/Ba plotting field (Fig. 3 a), and from Type IV by the Pb vs. Mn diagram (Fig. 4 b).

6. Conclusions

Based on microanalytical studies, we show that the term “rock varnish” needs to be subdivided into more specific categories. Here, we propose to subdivide rock varnish into five categories. The combination of “fingerprint” ratios (Mn/Ba, Al/Ni, Mn/REY, Mn/Ce, Mn/Pb, La_N/Yb_N, and Ce/Ce*), total REE contents, internal features, element distribution, and element composition can be used to distinguish the potential paleoclimate archive Type I varnish from other rock varnishes (Tables 5 and 6 in the appendix). An originally biogenic origin is suggested for all Type I, III, and IV varnishes, based on EPR measurements, with a faster growth rate, or more recent formation, for Type III varnish.

A high Ce/Ce* ratio and high REE enrichments are good indicators for slowly growing varnishes that had a long accumulation time and are therefore likely to be good paleoclimate archives representing long time periods (Bau et al., 2014). We found these varnishes only in arid and semi-arid deserts so far. However, not all varnishes falling into the category Type I can be used as potential paleoclimate archive, samples showing steep topographies of the host rock surface are inapplicable. As far as the first rock varnish record in the literature is concerned, which Alexander von Humboldt described more than 200 years ago, it is clear from his description that it is a river splash varnish, and therefore probably quite different from the dry rock varnishes, some of which may be used as paleoclimate archives. Von Humboldt’s varnish was probably of Type V, which we have shown to be very different from Type I varnishes.

The chemical composition and structures suggest different geneses for the different varnish types. This would also explain the mystery of the large reported differences in growth rate and thickness of rock varnishes described in the literature, as well as the dissent about the biogenic or abiotic origin of rock varnishes.

Acknowledgements

This work was supported by the Max Planck Graduate Center with the Johannes Gutenberg University Mainz (MPGC), the Max Planck Society, and King Saud University.

The ALS is supported by the Director, Office of Science, Office of Basic Energy Sciences, of the US Department of Energy under Contract DE-AC02-05CH11231. We thank the Helmholtz-Zentrum Berlin for the allocation of the synchrotron radiation beamtime at BESSY II. Sampling of desert varnish in Israel was conducted during a funded ExpeER project. We want to thank B. Macholdt for collecting the Mauritanian rock varnish, R. Livingston for providing the urban varnish from the Smithsonian Castle, B. E. DiGregorio for providing all river splash zone varnishes, and T. Liu for providing a rock varnish sample collected in Death Valley. The help of Hosam Tuffah, Mohammed Al-Huraish, and Ayed Al-Harthy during the field campaign in Saudi Arabia is gratefully acknowledged. We furthermore thank T. Laubscher for enabling and assisting sample taking at the Freiburger Münster, Maik Biegler who prepared the varnish thin- and thick-sections, and L. M. Otter for the dust sieving. Furthermore, we want to thank Jan Leitner and Antje Sorowka for conducting the SEM element maps.

References

Abollino, O., Aceto, M., Malandrino, M., Sarzanini, C. and Mentasti, E. (2003) Adsorption of heavy metals on Na-montmorillonite. Effect of pH and organic substances. Water research 37, 1619-1627.

Bau, M., Schmidt, K., Koschinsky, A., Hein, J., Kuhn, T. and Usui, A. (2014) Discriminating between different genetic types of marine ferro-manganese crusts and nodules based on rare earth elements and yttrium. Chemical Geology 381, 1-9.

Broecker, W.S. and Liu, T. (2001) Rock Varnish: Record of desert Wetness? GSA today August, 4-10.

Burns, R.G. and Brown, B.A. (1972) Nucleation and mineralogical controls on the composition of manganese nodules. Ferromanganese Deposits on the Ocean floor, 51-61.

DiGregorio, B.E. (2001) Rock varnish as a habitat for extant life on Mars, in: Hoover, R.B., Levin, G.V., Paepe, R.R., Rozanov, A.Y. (Eds.), Instruments, Methods, and Missions for Astrobiology Iv, pp. 120-130.

Dorn, R.I. (1984) Cause and implications of rock varnish microchemical laminations. Nature 310, 767-770.

Dorn, R.I. (2008) Rock Varnish in Geochemical sediments and landscapes. Eds. D. J. Nash and S. J. McLaren, Blackwell Publishing Ltd, Oxford, UK Chapter 8, 246-297.

Dorn, R.I. (2009) Desert rock coatings, in: Parsons, A.J.a.A., A.D (Ed.), Geomorphology of Desert Environments. Springer, Amsterdam, pp. 153-186.

Dorn, R.I., Krinsley, D.H., Liu, T.Z., Anderson, S., Clark, J., Cahill, T.A. and Gill, T.E. (1992) Manganese-rich Rock Varnish does occur in Antarctica. Chemical Geology 99, 289-298.

Engel, C.G. and Sharp, R.P. (1958) Chemical Data on Desert Varnish. Geological Society of America Bulletin 69, 487-&.

Evensen, N., Hamilton, P.J. and O'nions, R. (1978) Rare-earth abundances in chondritic meteorites. Geochimica et Cosmochimica Acta 42, 1199-1212.

Feng, X.H., Zhai, L.M., Tan, W.F., Liu, F. and He, J.Z. (2007) Adsorption and redox reactions of heavy metals on synthesized Mn oxide minerals. Environmental Pollution 147, 366-373.

Follath, R., Schmidt, J.S., Weigand, M. and Fauth, K. (2010) The X-ray microscopy beamline UE46-PGM2 at BESSY. Sri 2009: The 10th International Conference on Synchrotron Radiation Instrumentation. Eds: R. Garrett, I. Gentle, K. Nugent, S. Wilkins, 323-326.

Goldsmith, Y., Stein, M. and Enzel, Y. (2014) From dust to varnish: Geochemical constraints on rock varnish formation in the Negev Desert, Israel. Geochimica Et Cosmochimica Acta 126, 97-111.

Hodge, V.F., Farmer, D.E., Diaz, T. and Orndorff, R.L. (2005) Prompt detection of alpha particles from Po-210: another clue to the origin of rock varnish? Journal of Environmental Radioactivity 78, 331-342.

Jochum, K., Wilson, S., Becker, H., Garbe-Schönberg, D., Groschopf, N., Kadlag, Y., Macholdt, D., Mertz-Kraus, R., Otter, L. and Stoll, B. (2016) FeMnOx-1: A new microanalytical reference material for the investigation of Mn–Fe rich geological samples. Chemical Geology 432, 34-40.

Jochum, K.P., Stoll, B., Weis, U., Jacob, D.E., Mertz-Kraus, R. and Andreae, M.O. (2014) Non-Matrix-Matched Calibration for the Multi-Element Analysis of Geological and Environmental Samples Using 200 nm Femtosecond LA-ICP-MS: A Comparison with Nanosecond Lasers. Geostandards and Geoanalytical Research 38, 265-292.

Kijlstra, W.S., Poels, E.K., Bliek, A., Weckhuysen, B.M. and Schoonheydt, R.A. (1997) Characterization of Al2O3-supported manganese oxides by electron spin resonance and diffuse reflectance spectroscopy. The Journal of Physical Chemistry B 101, 309-316.

Kilcoyne, A.L.D., Tyliszczak, T., Steele, W.F., Fakra, S., Hitchcock, P., Franck, K., Anderson, E., Harteneck, B., Rightor, E.G., Mitchell, G.E., Hitchcock, A.P., Yang, L., Warwick, T. and Ade, H. (2003) Interferometer-controlled scanning transmission X-ray microscopes at the Advanced Light Source. Journal of Synchrotron Radiation 10, 125-136.

Kim, S.S., Bargar, J.R., Nealson, K.H., Flood, B.E., Kirschvink, J.L., Raub, T.D., Tebo, B.M. and Villalobos, M. (2011) Searching for biosignatures using electron paramagnetic resonance (EPR) analysis of manganese oxides. Astrobiology 11, 775-786.

Krinsley, D., Ditto, J., Langworthy, K., Dorn, R.I. and Thompson, T. (2013) Varnish microlaminations: new insights from focused ion beam preparation. Physical Geography 34, 159-173.

Krinsley, D.H., Dorn, R.I., DiGregorio, B.E., Langworthy, K.A. and Ditto, J. (2012) Rock varnish in New York: An accelerated snapshot of accretionary processes. Geomorphology 138, 339-351.

Lanza, N.L., Clegg, S.M., Wiens, R.C., McInroy, R.E., Newsom, H.E. and Deans, M.D. (2012) Examining natural rock varnish and weathering rinds with laser-induced breakdown spectroscopy for application to ChemCam on Mars. Applied Optics 51, B74-B82.

Lee, M.R. and Bland, P.A. (2003) Dating climatic change in hot deserts using desert varnish on meteorite finds. Earth and Planetary Science Letters 206, 187-198.

Li, X., Pan, G., Qin, Y., Hu, T., Wu, Z. and Xie, Y. (2004) EXAFS studies on adsorption–desorption reversibility at manganese oxide–water interfaces: II. Reversible adsorption of zinc on δ-MnO2. Journal of colloid and interface science 271, 35-40.

Liu, T.H. and Broecker, W.S. (2000) How fast does rock varnish grow? Geology 28, 183-186.

Livingston, R., Grissom, C., Vicenzi, E., Weldon-Yochim, Z., Little, N., Douglas, J., Fowler, A., Santelli, C., Macholdt, D. and Ortiz-Montalvo, D. (2016) Investigation of urban rock varnish on the sandstone of the Smithsonian Castle. Science and Art: A Future for Stone, 399.

Lozano, R.P. and Rossi, C. (2012) Exceptional preservation of Mn-oxidizing microbes in cave stromatolites (El Soplao, Spain). Sedimentary Geology 255, 42-55.

Lytle, C., Smith, B. and McKinnon, C. (1995) Manganese accumulation along Utah roadways: a possible indication of motor vehicle exhaust pollution. Science of the total environment 162, 105-109.

Macholdt, D., Jochum, K., Pöhlker, C., Stoll, B., Weis, U., Weber, B., Müller, M., Kappl, M., Buhre, S. and Kilcoyne, A. (2015) Microanalytical methods for in-situ high-resolution analysis of rock varnish at the micrometer to nanometer scale. Chemical Geology 411, 57-68.

Macholdt, D.S., Jochum, K.P., Stoll, B., Weis, U. and Andreae, M.O. (2014) A new technique to determine element amounts down to femtograms in dust using femtosecond laser ablation-inductively coupled plasma-mass spectrometry. Chemical Geology 383, 123-131.

Macholdt, D.S., Jochum, K.P., Wilson, S.A., Otter, L.M., Stoll, B., Weis, U. and Andreae, M.O. (2016) Suitability of Mn-and Fe-Rich Reference Materials for Microanalytical Research. Geostandards and Geoanalytical Research.

McKeown, D.A. and Post, J.E. (2001) Characterization of manganese oxide mineralogy in rock varnish and dendrites using X-ray absorption spectroscopy. American Mineralogist 86, 701-713.

Northup, D.E., Snider, J.R., Spilde, M.N., Porter, M.L., van de Kamp, J.L., Boston, P.J., Nyberg, A.M. and Bargar, J.R. (2010) Diversity of rock varnish bacterial communities from Black Canyon, New Mexico. Journal of Geophysical Research-Biogeosciences 115.

Nowinski, P., Hodge, V.F., Gerstenberger, S. and Cizdziel, J.V. (2013) Analysis of mercury in rock varnish samples in areas impacted by coal-fired power plants. Environmental Pollution 179, 132-137.

Ohta, A. and Kawabe, I. (2001) REE(III) adsorption onto Mn dioxide (delta-MnO2) and Fe oxyhydroxide: Ce(III) oxidation by delta-MnO2. Geochimica Et Cosmochimica Acta 65, 695-703.

Otter, L.M., Macholdt, D.S., Jochum, K.P., Stoll, B.,Weis, U., Weber, B., Al-Amrid, A.M., Haug, G.H., Andreae, M.O. (in preparation) Relationship between Rock Varnish and Adjacent Mineral Dust.

Pan, G., Qin, Y., Li, X., Hu, T., Wu, Z. and Xie, Y. (2004) EXAFS studies on adsorption–desorption reversibility at manganese oxides–water interfaces: I. Irreversible adsorption of zinc onto manganite (γ-MnOOH). Journal of colloid and interface science 271, 28-34.

Perry, R.S., Dodsworth, J., Staley, J.T. and Engel, M.H. (2004) Bacterial diversity in desert varnish, in: Harris, R.A., Ouwehand, L. (Eds.), Proceedings of the Iii European Workshop on Exo-Astrobiology: Mars: The Search for Life, pp. 259-260.

Perry, R.S. and Kolb, V.M. (2004) Biological and organic constituents of desert varnish: review and new hypotheses, in: Hoover, R.B., Rozanov, A.Y. (Eds.), Instruments, Methods, and Missions for Astrobiology Vii, pp. 202-217.

Perry, R.S., Kolb, V.M., Lynne, B.Y., Sephton, M.A., McLoughlin, N., Engel, M.H., Olendzenski, L., Brasier, M. and Staley, J.T. (2005) How desert varnish forms? Proceedings of the SPIE - The International Society for Optical Engineering 5906, 59060V-59061-59012.

Perry, R.S. and Sephton, M.A. (2006) Desert varnish: an environmental recorder for Mars. Astronomy & Geophysics 47, 34-35.

Potter, R.M. and Rossman, G.R. (1979) The Manganese- and iron-Oxide Mineralogy of Desert Varnish. Chemical Geology 25, 79-94.

Raymond, R., Guthrie, G., Bish, D., Reneau, S. and Chipera, S. (1993) Biomineralization of manganese in rock varnish. Catena Supplement 21, 321-321.

Reneau, S.L., Raymond, R. and Harrington, C.D. (1992) Elemental relationships in rock varnish stratigraphic layers, Cima Volcanic Field, California - Implications for varnish development and the interpretation of varnish chemistry. American Journal of Science 292, 684-723.

Rossi, C., Lozano, R.P., Isanta, N. and Hellstrom, J. (2010) Manganese stromatolites in caves: El Soplao (Cantabria, Spain). Geology 38, 1119-1122.

Rudnick, R.L. and Gao, S. (2003) 3.01 - Composition of the Continental Crust. Treatise On Geochemistry, Elsevier Ltd 3, 1-64.

Rybicka, E.H., Calmano, W. and Breeger, A. (1995) Heavy metals sorption/desorption on competing clay minerals; an experimental study. Applied Clay Science 9, 369-381.

Spilde, M.N., Boston, P. and Northrup, D. (2002) Subterranean manganese deposits in caves: Analogies to rock varnish. Geological Society of American Abstracts with Programs http://gsa. confex. com/gsa/2002AM/finalprogram/abstract 46060. htm.

Spilde, M.N., Melim, L.A., Northup, D.E. and Boston, P.J. (2013) Anthropogenic lead as a tracer of rock varnish growth: Implications for rates of formation. Geology 41, 263-266.

Tebo, B.M., Bargar, J.R., Clement, B.G., Dick, G.J., Murray, K.J., Parker, D., Verity, R. and Webb, S.M. (2004) Biogenic manganese oxides: Properties and mechanisms of formation. Annu Rev Earth Pl Sc 32, 287-328.

Tebo, B.M., Johnson, H.A., McCarthy, J.K. and Templeton, A.S. (2005) Geomicrobiology of manganese (II) oxidation. TRENDS in Microbiology 13, 421-428.

Thiagarajan, N. and Lee, C.T.A. (2004) Trace-element evidence for the origin of desert varnish by direct aqueous atmospheric deposition. Earth and Planetary Science Letters 224, 131-141.

Vicenzi, E.P., Grissom, C.A., Livingston, R.A., Weldon-Yochim, Z. (2016) Rock varnish on architectural stone: microscopy and analysis of nanoscale manganese oxide deposits on the Smithsonian Castle, Washington, DC. Heritage Science 4.

Von Humboldt, A. and Bonpland, A. (1819) Voyage aux régions équinoxiales du nouveau continent. II, 299-304.

Watchman, A. (2000) A review of the history of dating rock varnishes. Earth-Science Reviews 49, 261-277.

Appendix

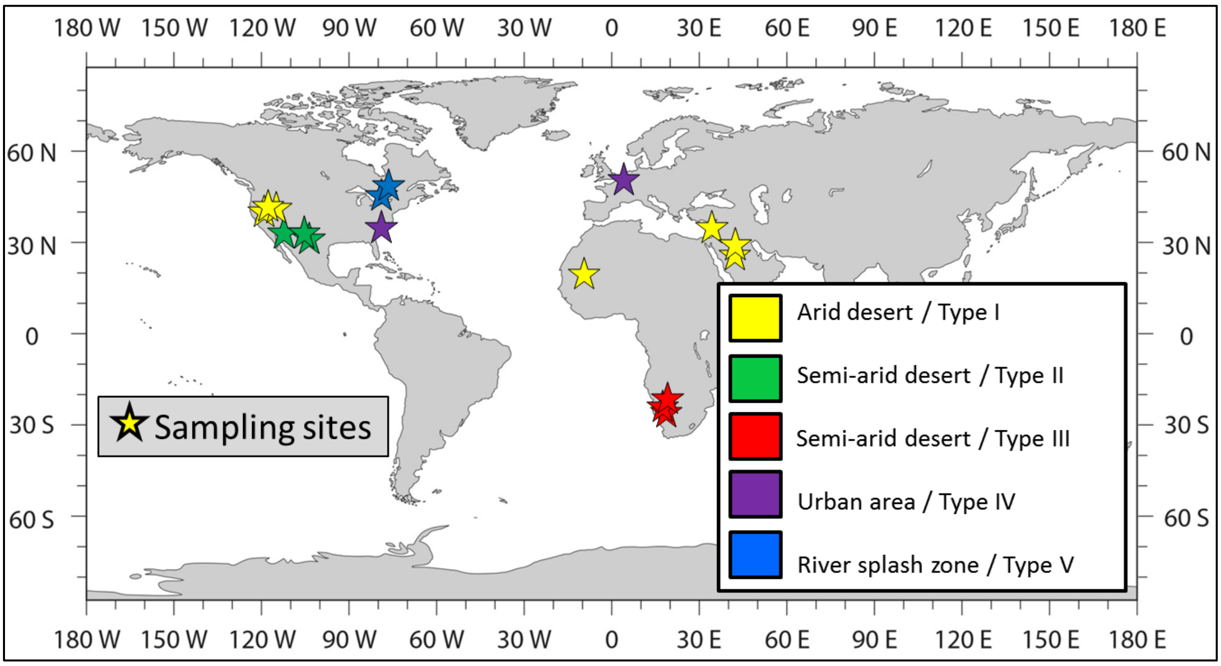

Figure A: Sampling locations of rock varnish. Yellow stars: Type I varnish; green stars: Type II varnish; red stars: Type III varnish; purple stars: Type IV varnish; blue stars: Type V varnish.

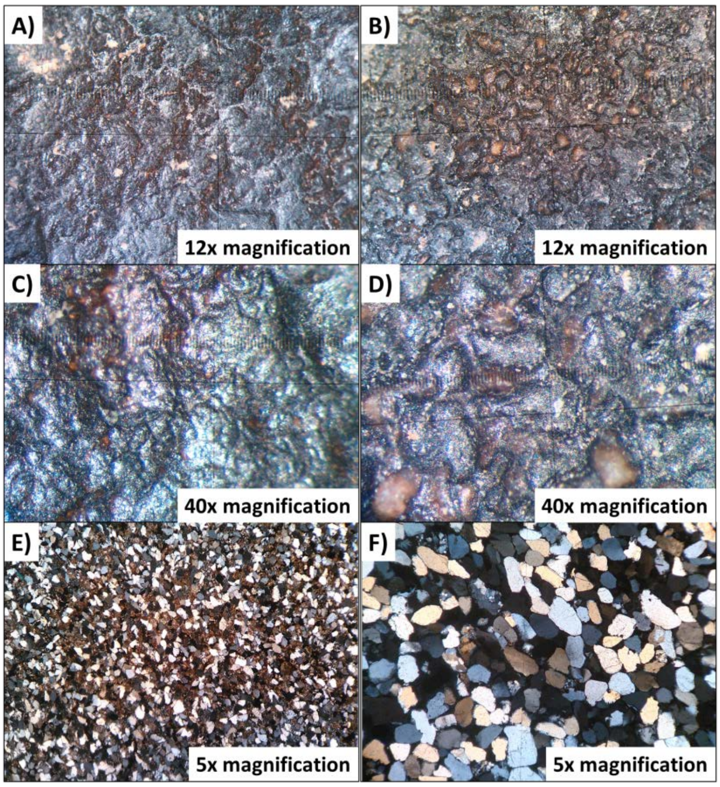

Figure B: Microscope images of two Saudi Arabian varnishes. A), C), E): Type I varnish from Yatib (AR14 Y1), B), D), F): Type I varnish from Jubbah (AR14 J1). Images A), B), C), and D) were taken as reflected light images from the surfaces of the varnishes with a conventional binocular microscope, images E), F) are transmission light polarization microscope images of the host rocks (sandstones) made of thin sections (25-30 µm).

.

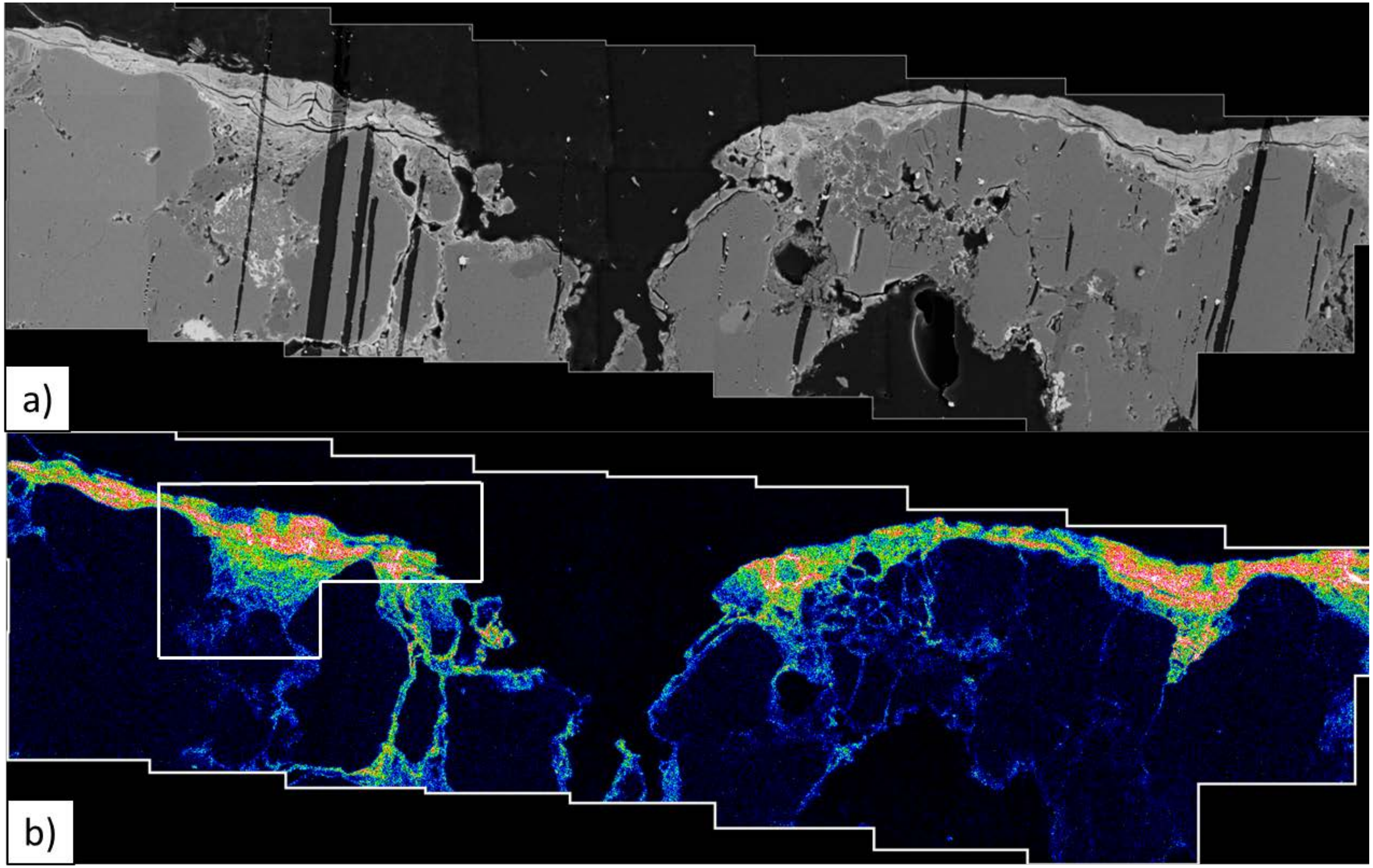

Figure C: Secondary electron microscopy (SEM) images of a varnish sample from Saudi Arabia, Yatib, collected from an almost vertical surface. Fig. C a) is an backscattered electron image, Fig.C b) is an EDX mapping of the element Mn. Layers are observable in both images.

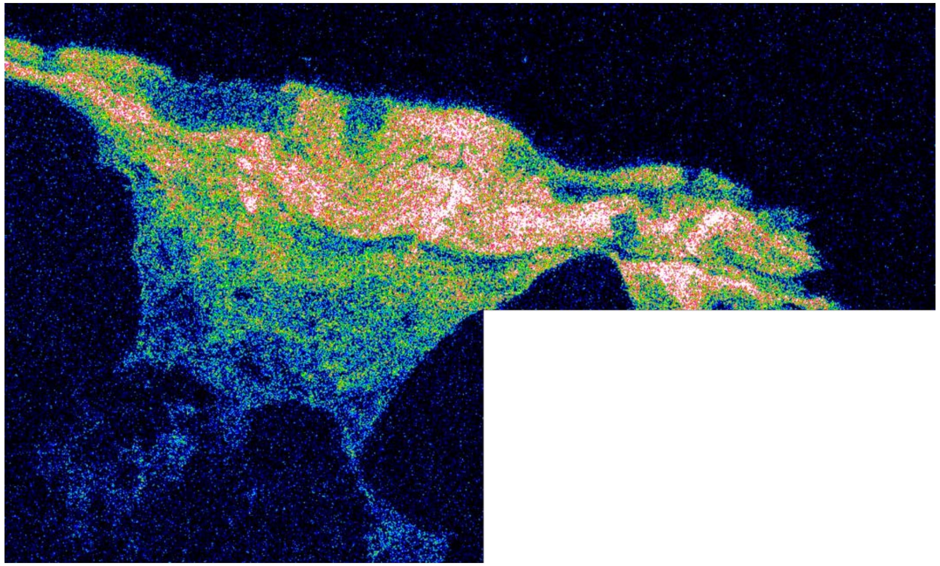

Figure D: Close up of marked area in Figure C b).

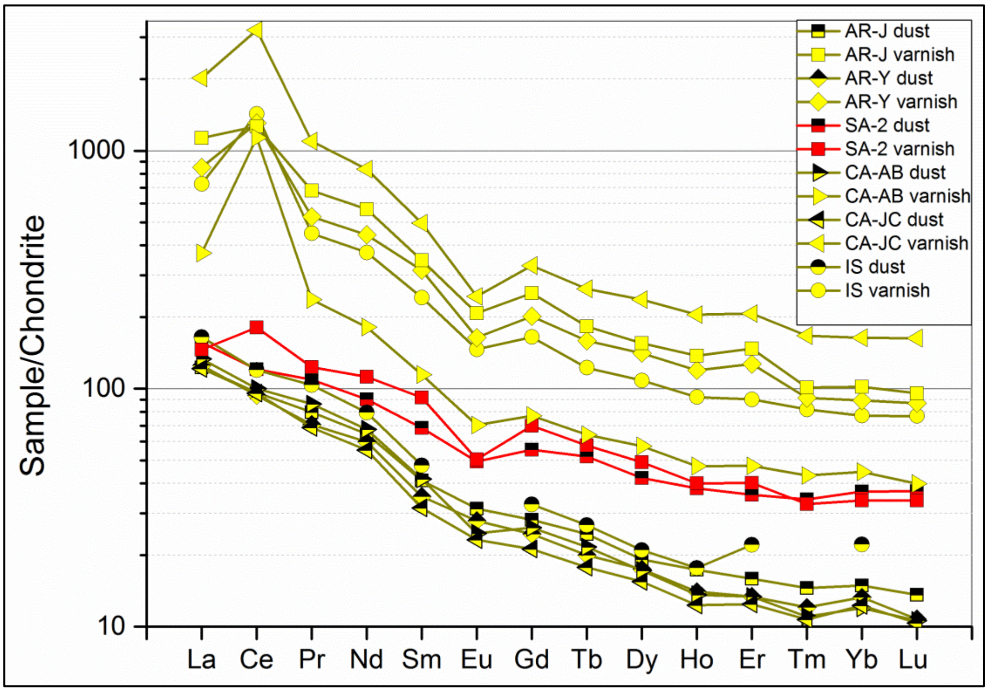

Figure E: CI chondrite normalized rare earth element patterns of varnish and fine sieved (< 50 µm) dust samples. Type I varnishes (yellow) show a significant enrichment of REEs relative to adjacent collected dust. Type III varnish (red) shows only a very small enrichment.

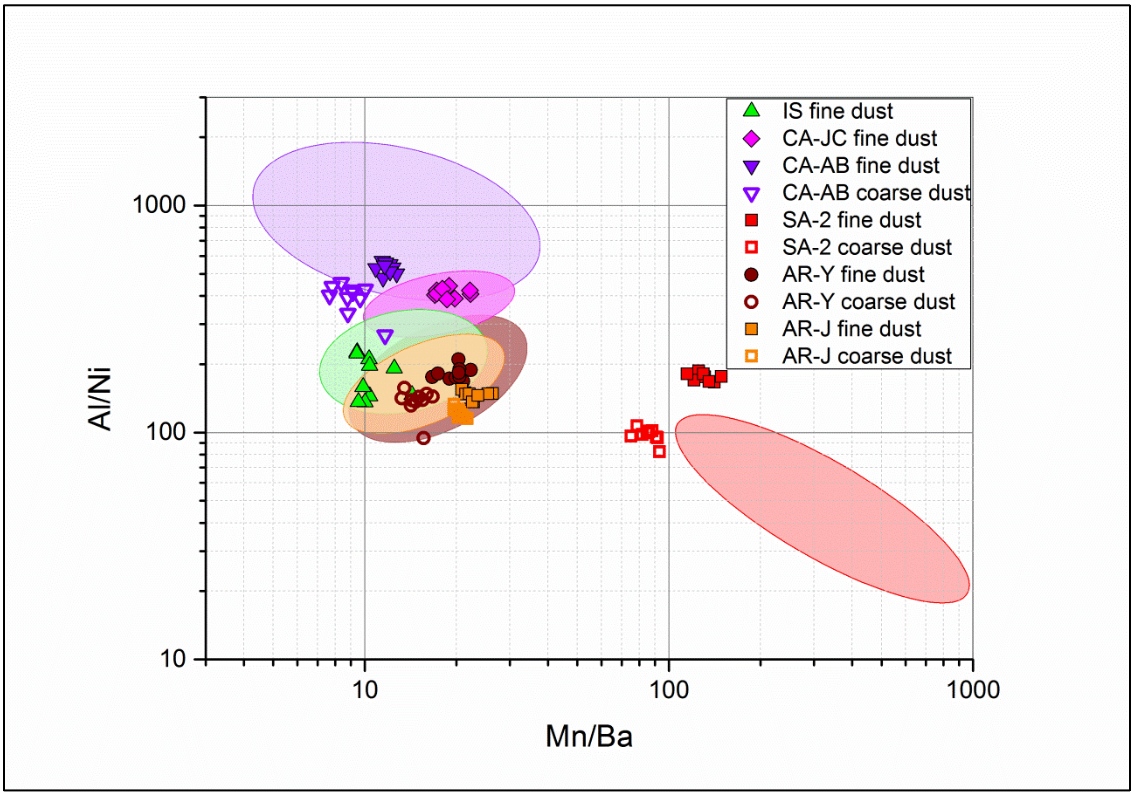

Figure F: Al/Ni vs. Mn/Ba ratio plot for dust fine fractions (<50 µm) and dust coarse fractions (≥50 µm, milled) from dust collected adjacent to varnish. Al/Ni and Mn/Ba dust ratios were multiplied by a fractionation factor of 0.2, and 9, respectively. The colored fields are the ranges where the corresponding rock varnishes plot for each equally colored dust sample. Purple, pink, green, orange, and brown fields: Type I varnishes; red colored field: Type III varnish.

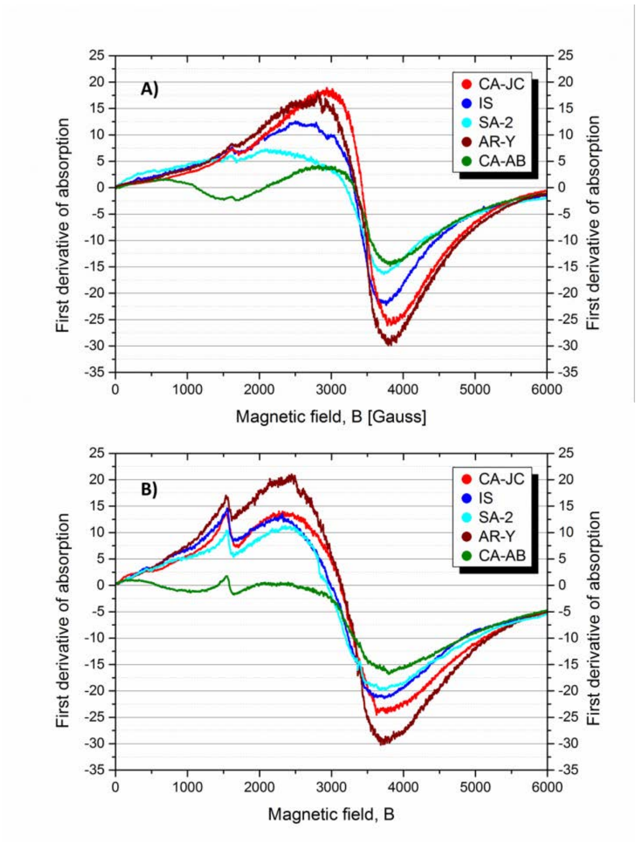

Figure G: Electron paramagnetic resonance spectra of five rock varnish samples. A) spectra measured at RT (293 K) and with 210 mW. B) spectra measured at 90 K and with 224 mW. In all spectra, a Fe^{3+} peak can be observed at about 1500 G on the flank of the relatively narrow (560-1200 G) Mn absorption peak.

Table 1: Varnish samples with information about their sampling location, underlying rock type, and environment.

Varnish Type	Sample Name	Country	Location	Rock Type	GPS Coordinates	# of samples	Environment
Type I	IS	Israel	Negev Desert, Sde Boker	Quartz-rimmed limestone	30°52’25.13”N 34°47’3.8”E	4	Arid desert
Type I	CA-JC	California, USA	Johnson Canyon	Magmatic and metamorphic	36°05'49.87''N 116°51'30.32''W	4	Arid desert
Type I	CA-MD	California, USA	Mojave Desert	Magmatic and metamorphic	See (Macholdt et al., 2015)	7	Arid desert
Type I	CA-AB	California, USA	Anza Borrego	Magmatic and metamorphic	33°17’4”N 116°8’2”W	3	Arid desert
Type I	CA-DV	California, USA	Death Valley	Magmatic and metamorphic	36°51'31''N 117°15'59''W Rest see (Macholdt et al., 2015)	5	Arid desert
Type I	MT	Mauritania	Azougui, Sahara	Sandstone	20°37'46.40"N 13° 8'15.44"W	1	Arid desert
Type I	AR-J	Saudi Arabia	Jubbah, An Nafud	Sandstone	28°01'54.51"N 40°55'5.67"E	6	Arid desert
Type I	AR-Y	Saudi Arabia	Yatib, An Nafud	Sandstone	27°29'22.40"N 41°58'35.19"E	6	Arid desert
Type II	SA-1	South Africa	Knersvlakte	Quartzite	31°16’45.2‘‘S 18°35’42.6‘‘E	8	Semi-arid desert
Type II	SA-2	South Africa	Knersvlakte	Quartzite	31°16'55.4''S 18°35'17.8''E	4	Semi-arid desert
Type III	TX FD 1	Texas, USA	Fort Davis, Chihuahuan Desert	Magmatic	30°36'6.48"N 103°54'46.8"W	1	Semi-arid desert
Type III	TX FD 2-4	Texas, USA	Fort Davis, Chihuahuan Desert	Magmatic	30°46'36''N 103°44'46''W	3	Semi-arid desert
Type III	TX FD 5-6	Texas, USA	Fort Davis, Chihuahuan Desert	Magmatic	30°39'36.72"N 103°47'31.56"W	2	Semi-arid desert
Type III	TX FD 7	Texas, USA	Fort Davis, Chihuahuan Desert	Magmatic	30°35'58.95"N 103°53'38.76"W	1	Semi-arid desert
Type III	AZ AL	Arizona, USA	Arizona, Alamo Canyon	Magmatic	32°4'19.92"N 112°43'42.96"W	1	Semi-arid desert
Type IV	SC	USA	Washington D.C, Smithsonian Castle, wall	Sandstone	38°53'19.63"N 77° 1'33.68"W	2	Urban varnish
Type IV	FM	Germany	Freiburger Münster, Freiburg, wall	Sandstone	47°59'43.52"N 7°51'11.85"E	1	Urban varnish
Type V	R River	NY State, USA	Adirondack Raquette River, South Colton	Gneiss	44°30'31.24"N 74°53'5.16"W	1	River splash zone
Type V	E Canal	NY State, USA	Erie Barge Canal, Middleport	Sandstone	43°12'42.09"N 78°28'43.23"W	1	River splash zone

Table 2: Operating parameters used for the fs laser ablation system.

	NWRFemto
Laser type	Ti:Sapphire
Wavelength [nm]	200
Pulse length [fs]	150
Energy density [J cm^{-2}]	0.3
Spot size [µm]	40
Pulse repetition rate [Hz]	50
Scan time [s]	350
Scan speed [µm s^{-1}]	1
Warmup and blank measurement [s]	15
Washout [s]	30

Table 3: Operating parameters of the Element2 ICP-MS.

rf power [W]	1270
Cooling gas flow rate [l min^{-1}]	15
Auxiliary gas flow rate [l min^{-1}]	1
Carrier gas (Ar) flow rate [l min^{-1}]	0.8
Carrier gas (He) flow rate [l min^{-1}]	0.7
Sample time [s]	0.002
Samples per peak	25
Mass window [%]	40
Time per pass [s]	1.4
Mass resolution	2000
Measuring type	Both; E-scan and counting mode

Table 4: fs ICP-MS results of all samples, including the relative standard deviation (RSD).

		CA-DV						CA-JC							
Element	Isotope used	CA14 DV10		CA14 DV11		CA14 DV12		CA14 JC1		CA14 JC4		CA14 JC9		CA14 JC8	
		[µg g^{-1}]	RSD [%]	[µg g^{-1}]	RSD [%]	[µg g^{-1}]	RSD [%]	[µg g^{-1}]	RSD [%]	[µg g^{-1}]	RSD [%]	[µg g^{-1}]	RSD [%]	[µg g^{-1}]	RSD [%]
Na	Na^{23}	3996	9	6251	53	12626	33	3279	23	4912	47	11871	40	874	39
Mg	Mg^{25}	12833	19	15117	31	12913	24	19636	24	14493	29	10978	20	15085	22
Al	Al^{27}	99401	12	101653	9	90414	12	111806	5	90491	18	111871	10	78465	17
Si	Si^{29}	154146	10	149495	12	172347	16	167231	17	195085	16	198256	10	223625	14
P	P^{31}	7720	24	19627	26	12977	18	7693	28	6237	17	5354	23	13065	27
K	K^{39}	20263	29	16500	14	17214	29	19360	24	13369	39	29317	32	10641	20
Ca	Ca^{43}	11573	24	22460	37	37534	25	13695	26	10519	21	7769	15	30748	36
Ti	Ti^{47}	3712	33	5423	24	3435	18	6166	40	3054	38	4208	35	7039	44
V	V^{51}	227	18	180	17	157	32	208	11	165	19	157	15	454	38
Cr	Cr^{53}	66	38	59	33	40	26	78	21	59	30	58	9	118	16
Mn	Mn^{55}	141238	26	123935	24	120168	26	88468	41	95997	16	83034	30	69117	21
Fe	Fe^{57}	91031	29	92667	14	71724	20	99729	20	82939	23	73501	15	79626	11
Co	Co^{59}	684	24	404	18	444	16	394	30	435	22	330	22	567	24
Ni	Ni^{60}	372	23	225	32	214	16	328	20	250	22	223	8	523	21
Cu	Cu^{63}	370	32	141	26	145	21	267	27	229	16	239	43	299	17
Zn	Zn^{67}	761	36	440	23	368	23	367	23	311	23	233	8	819	25
Rb	Rb^{85}	124	20	103	27	99	17	134	21	88	36	182	42	61	14
Sr	Sr^{88}	732	30	745	24	1391	17	543	42	666	29	392	27	745	34
Y	Y^{89}	518	30	162	21	154	25	253	26	237	20	236	36	203	22

Zr	Zr^{90}	290	17	356	15	299	24	286	14	273	35	224	29	243	8
Cs	Cs^{133}	14	27	11	35	9.1	27	13	14	8.6	30.5	9.1	35	4.2	11.2
Ba	Ba^{138}	9826	30	7265	28	9953	20	8072	49	5369	34	3653	30	7334	18
La	La^{139}	1089	29	305	30	317	28	491	28	495	18	445	28	309	24
Ce	Ce^{140}	3297	18	2010	34	1856	27	1751	28	2048	25	1817	23	1064	21
Pr	Pr^{141}	224	26	72	32	73	31	104	28	106	20	94	33	73	22
Nd	Nd^{143}	891	26	276	30	282	31	404	28	396	19	380	28	305	22
Sm	Sm^{147}	172	24	54	29	52	30	78	28	76	22	75	26	60	21
Eu	Eu^{151}	32	24	10	27	10	25	14	27	14	23	13	29	13	20
Gd	Gd^{157}	164	26	47	26	47	27	70	27	67	24	71	28	55	22
Tb	Tb^{159}	22	21	6.7	25	6.4	29	10	27	10	24	10	36	7.7	20.8
Dy	Dy^{161}	124	22	39	23	38	26	59	27	60	26	57	34	46	22
Ho	Ho^{165}	25	25	7.7	24	6.9	23	12	24	12	26	11	21	8.6	20.2
Er	Er^{167}	71	23	23	23	21	28	34	22	34	25	35	22	27	22
Tm	Tm^{169}	8.9	19	2.9	23	2.7	30	4.7	23	4.3	29.6	4.4	23	3.0	23.2
Yb	Yb^{173}	58	16	17	22	17	28	28	22	27	25	28	26	18	21
Lu	Lu^{175}	8.2	16	2.6	21	2.6	27	4.4	19	4.1	25.0	4.0	28	2.7	22.1
Pb	Pb^{208}	3651	22	761	23	463	33	558	24	1342	36	1781	16	278	20
Th	Th^{232}	281	36	120	25	107	25	80	33	128	28	121	38	34	30
U	U^{238}	36	22	25	20	17	27	38	24	53	34	23	12	13	22

Tabelle 4: Continued

		CA-AB						IS		SA-1			
Element	Isotope used	CA13 ABD-2		CA13 ABD-3		CA13 ABD-5		IS13 V3		SA10 #10		SA10 #11	
		[µg g^{-1}]	RSD [%]	[µg g^{-1}]	RSD [%]	[µg g^{-1}]	RSD [%]	[µg g^{-1}]	RSD [%]	[µg g^{-1}]	RSD [%]	[µg g^{-1}]	RSD [%]
Na	Na^{23}	2149	41	593	52	937	35	2857	18	11940	44	5049	14
Mg	Mg^{25}	17303	24	43533	45	29954	35	15895	20	7442	30	9087	14
Al	Al^{27}	84668	21	109732	26	84811	21	96228	16	37580	18	33637	14
Si	Si^{29}	222301	17	195011	18	196353	5	211422	19	182893	32	142189	20
P	P^{31}	6021	31	789	24	4276	22	2920	23	3174	27	2878	17
K	K^{39}	13193	50	71939	10	11671	35	13060	15	18728	35	24969	15
Ca	Ca^{43}	23241	36	3134	28	39192	44	17387	14	17590	18	14417	6
Ti	Ti^{47}	5239	51	10343	45	4433	24	4936	23	1770	41	2007	24
V	V^{51}	146	41	309	36	400	14	275	12	84	25	73	14
Cr	Cr^{53}	8.2	53.8	197	56	140	36	146	12	44	32	51	15
Mn	Mn^{55}	31187	37	21823	19	71898	34	83123	31	202776	42	309039	12
Fe	Fe^{57}	96513	33	98189	43	100235	16	90403	14	35077	31	28462	22
Co	Co^{59}	276	41	115	28	395	32	699	23	1308	47	1596	19
Ni	Ni^{60}	113	42	175	40	274	22	513	30	268	32	286	24
Cu	Cu^{63}	120	26	93	20	325	32	189	25	151	28	90	22
Zn	Zn^{67}	256	31	283	39	449	35	429	13	533	29	659	19
Rb	Rb^{85}	77	39	350	34	70	28	78	14	76	20	97	12
Sr	Sr^{88}	265	40	225	30	478	33	574	23	946	30	611	29
Y	Y^{89}	61	32	13	23	158	28	171	21	108	31	79	18
Zr	Zr^{90}	60	47	29	32	85	19	270	13	92	22	67	20
Cs	Cs^{133}	7.1	42.4	33	34	7.3	24	4.6	17	3.8	21	6.0	35

Ba	Ba^{138}	2721	31	12806	34	9290	39	8986	26	1379	36	861	34
La	La^{139}	94	31	74	31	274	33	235	21	45	25	25	21
Ce	Ce^{140}	900	47	273	20	1118	46	1608	23	109	31	79	20
Pr	Pr^{141}	25	38	12	34	60	27	62	20	17	18	12	30
Nd	Nd^{143}	93	39	35	32	232	26	253	21	87	11	68	28
Sm	Sm^{147}	18	34	6.7	35.2	45	25	54	20	25	14	20	28
Eu	Eu^{151}	4.1	33.7	2.0	22.0	10	24	12	21	5.4	21	4.6	27
Gd	Gd^{157}	16	33	7.0	34.4	50	26	51	20	30	26	23	21
Tb	Tb^{159}	2.8	42.8	0.9	28.8	6.3	24	7.0	20	4.9	26	3.4	20
Dy	Dy^{161}	15	34	4.7	30.1	36	24	42	22	26	28	19	22
Ho	Ho^{165}	2.7	34.1	0.91	24.97	6.6	26	7.9	19	5.3	30	3.8	21
Er	Er^{167}	10	40	2.3	31.4	18	26	23	20	17	35	11	20
Tm	Tm^{169}	1.2	43.4	0.33	36.32	2.3	23	3.0	20	1.9	32	1.4	22
Yb	Yb^{173}	8.6	39.3	1.9	31.5	15	18	18	19	12	31	8.3	23
Lu	Lu^{175}	1.1	29.7	0.29	38.00	2.2	23	2.7	19	1.9	28	1.2	25
Pb	Pb^{208}	1075	41	582	33	1252	41	491	32	103	36	55	32
Th	Th^{232}	8.3	39.3	6.2	29.5	24	26	27	25	16	31	13	33
U	U^{238}	14	39	3.3	32.3	22	34	5.7	15	5.3	33	4.7	20

Tabelle 4: Continued

		SC		FM		MT		SA-2							
Element	Isotope used	Livingston		FM965		MT		SA14 DV05a		SA14 DV05b		SA14 DV09a		SA14 DV09b	
		[µg g^{-1}]	RSD [%]	[µg g^{-1}]	RSD [%]	[µg g^{-1}]	RSD [%]	[µg g^{-1}]	RSD [%]	[µg g^{-1}]	RSD [%]	[µg g^{-1}]	RSD [%]	[µg g^{-1}]	RSD [%]
Na	Na^{23}	3197	69	1839	42	717	37	1311	15	1146	18	1632	16	1104	32
Mg	Mg^{25}	12070	20	3515	34	14025	7	4451	33	10082	18	7190	32	12428	17
Al	Al^{27}	28811	31	43563	26	93871	5	24936	21	57552	21	47351	28	49493	25
Si	Si^{29}	261636	26	252571	18	204608	5	168961	40	193074	21	212219	33	149422	29
P	P^{31}	357	20	25868	50	6798	21	3729	33	4154	19	4410	38	2939	11
K	K^{39}	5339	21	20445	26	25800	6	28141	38	31064	21	23034	32	27144	15
Ca	Ca^{43}	18030	40	20114	28	20985	14	5295	33	5573	25	6514	28	12644	17
Ti	Ti^{47}	3077	41	1545	23	6465	11	881	27	3052	32	1340	44	3260	45
V	V^{51}	248	38	83	37	194	6	66	23	129	20	109	41	107	26
Cr	Cr^{53}	82	38	64	22	110	10	33	20	75	24	80	39	74	28
Mn	Mn^{55}	80650	41	77108	39	84442	11	286141	32	195456	28	219989	25	259669	32
Fe	Fe^{57}	41345	39	29124	30	84010	10	18290	20	48982	19	55637	33	43414	25
Co	Co^{59}	187	17	525	71	731	14	1993	35	1471	18	991	23	733	17
Ni	Ni^{60}	114	33	286	39	311	15	80	33	451	32	381	29	921	27
Cu	Cu^{63}	1177	55	328	28	178	8	91	31	271	31	305	39	350	41
Zn	Zn^{67}	326	43	5000	36	2697	14	87	38	286	29	228	17	582	24
Rb	Rb^{85}	40	31	83	31	134	7	49	16	122	28	68	26	82	20
Sr	Sr^{88}	349	36	510	28	560	22	430	25	447	28	603	50	706	17
Y	Y^{89}	15	17	17	28	133	13	44	22	142	21	33	35	43	17
Zr	Zr^{90}	36	26	35	38	168	18	34	28	137	27	90	31	91	34
Cs	Cs^{133}	2.2	28	11	23	8.5	7	2.8	19	7.5	28	5.1	24	5.3	26

Ba	Ba^{138}	2537	28	1747	27	11245	19	634	32	1473	35	832	53	987	25
La	La^{139}	41	42	20	51	204	15	25	16	62	33	21	31	36	34
Ce	Ce^{140}	157	35	42	33	851	12	102	15	214	32	83	26	115	30
Pr	Pr^{141}	6.2	44	5.3	48	57	13	9	16	20	27	8	39	12	26
Nd	Nd^{143}	30	42	20	41	230	15	45	21	107	27	37	38	53	25
Sm	Sm^{147}	4.6	22	4.6	36	47	12	12	24	31	29	10	34	14	23
Eu	Eu^{151}	1.2	54	1.1	28	11	14	2.4	26	6.1	26	2.2	35	2.9	19
Gd	Gd^{157}	4.2	27	4.9	23	43	14	12	24	31	24	12	21	14	20
Tb	Tb^{159}	0.70	34	0.73	37	5.3	12	1.9	29	5.1	25	1.6	20	2.2	21
Dy	Dy^{161}	3.3	39	4.4	37	29	10	10	29	30	23	10	36	12	20
Ho	Ho^{165}	0.58	41	0.81	31	5.4	9	2.0	26	5.8	21	1.9	32	2.3	21
Er	Er^{167}	2.4	38	2.4	30	14	10	5.1	23	17	20	5.4	30	6.7	21
Tm	Tm^{169}	0.45	45	0.31	29	1.8	11	0.70	24	2.2	22	0.73	36	0.84	27
Yb	Yb^{173}	2.5	33	2.2	39	11	9	3.9	24	13	24	4.8	25	5.6	19
Lu	Lu^{175}	0.34	42	0.28	39	1.5	10	0.60	17	2.0	19	0.68	20	0.86	28
Pb	Pb^{208}	2762	24	8299	30	312	25	36	50	105	38	107	38	88	30
Th	Th^{232}	10	45	7.0	34	21	19	7.3	22	22	25	16	28	17	28
U	U^{238}	3.4	47	3.3	23	12	11	2.6	32	7.1	25	10	37	5.1	24

Tabelle 4: Continued

		AR-Y											
Element	Isotope used	AR14 Y5-3		AR14 Y4a		AR14 Y3		AR14 Y2b		AR14 Y2a		AR14 Y1	
		[µg g^{-1}]	RSD [%]	[µg g^{-1}]	RSD [%]	[µg g^{-1}]	RSD [%]	[µg g^{-1}]	RSD [%]	[µg g^{-1}]	RSD [%]	[µg g^{-1}]	RSD [%]
Na	Na^{23}	374	24	381	59	485	41	482	21	590	25	198	33
Mg	Mg^{25}	18441	19	7597	39	8887	40	12180	35	5588	36	7950	48
Al	Al^{27}	101429	9	47063	25	83164	35	69475	25	63915	43	80198	29
Si	Si^{29}	193070	10	278634	12	245347	21	258207	26	293946	19	275291	19
P	P^{31}	8050	11	7931	29	21096	44	6550	29	6310	35	9638	36
K	K^{39}	12648	17	5726	31	5862	46	9922	33	5084	41	6843	44
Ca	Ca^{43}	13979	24	20745	25	33491	47	11437	37	9202	26	10965	35
Ti	Ti^{47}	7052	23	3243	45	2725	30	3706	27	2204	36	2856	54
V	V^{51}	267	11	189	33	170	37	235	34	208	35	169	33
Cr	Cr^{53}	134	13	62	36	65	37	108	29	67	43	66	44
Mn	Mn^{55}	80700	21	49700	64	50234	42	41654	19	47755	43	43227	49
Fe	Fe^{57}	104729	12	60066	35	52641	37	70527	22	53060	32	56718	44
Co	Co^{59}	625	20	579	5	267	26	377	38	433	43	528	42
Ni	Ni^{60}	801	18	313	48	484	46	400	44	362	32	375	36
Cu	Cu^{63}	285	12	214	39	156	41	147	42	138	35	132	31
Zn	Zn^{67}	1143	13	540	42	781	41	288	43	217	34	226	16
Rb	Rb^{85}	73	19	30	38	32	47	55	33	29	42	37	45
Sr	Sr^{88}	586	21	908	19	685	31	332	44	435	45	308	44
Y	Y^{89}	319	15	183	29	250	36	158	29	151	35	172	29
Zr	Zr^{90}	333	18	258	22	163	34	226	24	196	26	216	21
Cs	Cs^{133}	6.4	19	2.8	32	2.5	42	3.9	27	2.5	42	3.5	32

Ba	Ba^{138}	4787	21	8683	39	6231	38	2229	35	2290	46	2078	41
La	La^{139}	472	14	372	20	324	25	209	35	207	36	208	29
Ce	Ce^{140}	1401	22	1433	28	702	26	990	23	677	38	968	35
Pr	Pr^{141}	110	15	86	24	73	25	52	33	50	32	53	28
Nd	Nd^{143}	449	16	354	23	307	26	213	32	208	31	223	28
Sm	Sm^{147}	90	16	70	26	60	24	48	30	49	35	51	36
Eu	Eu^{151}	19	15	14	22	14	26	9	33	10	34	11	27
Gd	Gd^{157}	82	15	61	18	59	26	40	25	42	34	45	30
Tb	Tb^{159}	11	15	8.3	24	7.9	27	5.4	26	6.4	34	6.4	31
Dy	Dy^{161}	67	15	37	47	45	29	34	30	37	31	38	28
Ho	Ho^{165}	13	16	7.1	37	9.0	27	6.7	28	6.8	32	6.9	24
Er	Er^{167}	35	14	18	35	32	34	18	25	23	35	23	29
Tm	Tm^{169}	4.7	16	2.4	22	3.1	33	2.2	19	2.5	31	2.1	25
Yb	Yb^{173}	30	14	18	24	19	32	15	23	15	33	14	27
Lu	Lu^{175}	4.4	17	2.9	21	2.6	26	2.1	25	2.3	31	2.1	24
Pb	Pb^{208}	312	25	626	23	312	43	250	29	228	33	191	36
Th	Th^{232}	43	17	38	48	21	40	25	28	27	23	34	25
U	U^{238}	21	16	7.1	41	17	34	11	22	12	31	13	33

Tabelle 4: Continued

		AR-J											
Element	Isotope used	AR14J2-4		AR14 J2-3		AR14 J2-2		AR14 J2		AR14 J1		AR14 J1a	
		[µg g^{-1}]	RSD [%]	[µg g^{-1}]	RSD [%]	[µg g^{-1}]	RSD [%]	[µg g^{-1}]	RSD [%]	[µg g^{-1}]	RSD [%]	[µg g^{-1}]	RSD [%]
Na	Na^{23}	443	20	499	24	734	47	846	39	273	38	408	32
Mg	Mg^{25}	13627	29	17878	27	16365	32	14947	22	11022	35	18689	21
Al	Al^{27}	66167	46	87870	19	64398	22	78201	17	68222	32	90252	25
Si	Si^{29}	186855	5	227918	18	249522	22	228107	14	268399	19	266314	17
P	P^{31}	24537	1	14349	38	14676	51	12608	27	15274	39	8554	28
K	K^{39}	11263	4	12410	25	10566	32	10351	20	10375	40	13415	32
Ca	Ca^{43}	40814	16	33798	37	26332	35	29809	36	18317	37	8257	45
Ti	Ti^{47}	5631	13	5571	32	3938	31	6637	44	4381	37	6677	24
V	V^{51}	186	55	233	19	209	25	435	38	193	29	163	25
Cr	Cr^{53}	88	46	113	24	99	19	117	16	93	37	116	28
Mn	Mn^{55}	67552	54	54303	15	49295	37	67731	21	48351	46	33916	29
Fe	Fe^{57}	63960	52	74003	17	61379	28	77730	11	58363	31	66414	23
Co	Co^{59}	524	48	383	16	381	16	563	24	341	47	251	42
Ni	Ni^{60}	588	39	610	34	438	36	489	21	427	30	321	34
Cu	Cu^{63}	136	56	187	16	180	32	279	17	129	44	168	31
Zn	Zn^{67}	1006	26	774	35	653	34	793	25	588	47	474	25
Rb	Rb^{85}	57	53	76	27	63	29	60	14	60	35	69	32
Sr	Sr^{88}	687	39	734	20	700	36	749	34	460	35	234	33
Y	Y^{89}	192	49	189	16	167	28	200	22	157	25	114	30
Zr	Zr^{90}	182	55	221	19	216	31	242	8	202	38	180	24
Cs	Cs^{133}	4.5	47	6.5	32	5.1	29	4.2	11	4.3	32	5.6	21

Ba	Ba^{138}	6535	48	3958	29	5862	44	7482	18	4920	57	1931	30
La	La^{139}	327	42	277	15	260	29	304	24	217	25	128	30
Ce	Ce^{140}	1134	42	808	17	778	16	1066	21	691	30	387	48
Pr	Pr^{141}	78	45	65	14	58	32	72	22	50	30	31	34
Nd	Nd^{143}	313	46	270	13	239	32	300	22	206	29	131	32
Sm	Sm^{147}	62	45	53	12	46	33	59	21	41	30	28	31
Eu	Eu^{151}	14	45	12	11	10	30	13	20	8.8	29	6.3	33
Gd	Gd^{157}	64	44	51	11	45	30	55	22	39	29	27	33
Tb	Tb^{159}	7.9	50	6.8	11	5.7	33	7.6	21	5.1	30	3.8	36
Dy	Dy^{161}	46	50	39	13	34	31	45	22	30	32	23	33
Ho	Ho^{165}	8.2	51	7.8	10	6.5	32	8.5	20	5.9	28	4.7	33
Er	Er^{167}	21	51	25	10	20	31	26	22	15	28	13	32
Tm	Tm^{169}	3.0	47	2.6	15	2.3	34	3.0	23	2.0	32	1.7	31
Yb	Yb^{173}	18	51	17	14	14	32	17	21	13	30	11	31
Lu	Lu^{175}	2.6	41	2.4	17	2.0	34	2.7	22	2.0	33	1.6	33
Pb	Pb^{208}	478	4	376	25	434	34	291	20	156	19	102	48
Th	Th^{232}	37	31	22	24	24	39	35	30	21	40	19	25
U	U^{238}	11	38	16	23	13	18	13	22	12	15	11	33

Tabelle 4: Continued

		TX FD													
Element	Isotope used	TX FD 1		TX FD 2		TX FD 3		TX FD 4		TX FD 5		TX FD 6		TX FD 7	
		[µg g^{-1}]	RSD [%]	[µg g^{-1}]	RSD [%]	[µg g^{-1}]	RSD [%]	[µg g^{-1}]	RSD [%]	[µg g^{-1}]	RSD [%]	[µg g^{-1}]	RSD [%]	[µg g^{-1}]	RSD [%]
Na	Na^{23}	3668	36	1059	26	403	16	1962	39	5039	23	5776	45	4198	36
Mg	Mg^{25}	6408	26	8978	26	8034	17	6532	32	2720	40	6775	45	3447	47
Al	Al^{27}	80849	18	40675	19	89833	11	69058	30	75923	9	72262	29	82208	17
Si	Si^{29}	200653	14	62855	17	120040	12	171717	11	244737	13	230105	18	241112	22
P	P^{31}	4821	43	2953	7	9608	21	6571	30	4611	40	2212	48	5563	39
K	K^{39}	32085	17	10344	23	15091	12	27352	26	40288	20	25638	32	32824	37
Ca	Ca^{43}	13090	30	17731	21	12370	20	9003	24	4601	32	10248	40	3732	31
Ti	Ti^{47}	3224	37	1155	27	5250	23	4879	39	5613	52	5145	29	3486	35
V	V^{51}	24	35	352	11	123	16	50	46	36	39	114	33	52	43
Cr	Cr^{53}	7.5	37	4.7	36	45	18	33	29	5	67	23	37	19	37
Mn	Mn^{55}	109688	32	402117	6	203053	20	145729	17	48148	34	43269	50	57031	49
Fe	Fe^{57}	65938	43	38903	15	99958	20	114244	23	76479	26	135430	45	65987	34
Co	Co^{59}	77	36	50	24	469	17	28	51	76	43	118	54	129	44
Ni	Ni^{60}	48	32	132	22	176	18	59	35	48	46	59	39	27	13
Cu	Cu^{63}	47	42	231	14	124	21	90	22	35	33	63	39	44	34
Zn	Zn^{67}	4364	23	741	15	2144	28	728	42	914	18	1148	40	933	45
Rb	Rb^{85}	178	15	30	21	94	15	188	22	152	13	174	33	174	32
Sr	Sr^{88}	375	29	1797	23	431	21	315	22	91	25	127	45	137	38
Y	Y^{89}	159	26	62	13	105	10	95	42	154	22	145	24	123	42
Zr	Zr^{90}	308	47	1161	29	379	22	1076	53	2193	46	1359	34	536	48
Cs	Cs^{133}	4.3	29	3	26	10	15	12	17	4	31	6	40	5.8	40

Ba	Ba^{138}	2711	32	39724	11	10419	21	9884	23	1141	52	3907	43	1804	57
La	La^{139}	132	22	208	12	185	13	112	43	206	29	234	38	159	37
Ce	Ce^{140}	1229	32	2910	22	1622	12	993	31	593	30	1419	49	799	29
Pr	Pr^{141}	31	25	43	14	48	11	27	46	43	29	53	36	39	33
Nd	Nd^{143}	118	28	168	12	193	12	122	42	179	29	204	33	149	34
Sm	Sm^{147}	25	25	35	13	41	16	27	44	37	36	40	35	29	29
Eu	Eu^{151}	2.5	29	1.7	15	6.2	13	2.7	45	3.4	35	3.3	38	2.6	44
Gd	Gd^{157}	26	27	27	14	36	20	34	26	34	21	33	33	29	36
Tb	Tb^{159}	3.9	24	3.4	20	4.9	15	3.6	39	4.6	21	4.8	30	4.2	37
Dy	Dy^{161}	26	23	21	22	29	19	23	43	30	26	32	24	28	40
Ho	Ho^{165}	5.1	23	3.5	13	5.4	21	4.2	42	6.0	25	6.3	23	5.7	40
Er	Er^{167}	16	28	8	10	14	12	14	24	20	24	20	21	16	36
Tm	Tm^{169}	2.4	33	1.2	10	2.1	11	2.2	41	3.0	30	3.0	31	2.2	33
Yb	Yb^{173}	17	38	8	8	14	21	15	46	16	25	21	23	15	31
Lu	Lu^{175}	2.3	40	1.3	15	2.0	21	2.2	44	2.5	13	3.0	24	2.4	31
Pb	Pb^{208}	505	33	242	42	1133	36	40	49	259	32	1019	34	706	41
Th	Th^{232}	29	37	13	40	66	16	24	38	32	37	38	30	44	31
U	U^{238}	4.8	36	5.4	11	7.3	23	4.9	40	4.4	32	6.1	26	8.8	32

Tabelle 4: Continued

		R River		E Canal		AZ AC	
Element	Isotope used	R River		E Canal		AZ AC	
		[µg g^{-1}]	RSD [%]	[µg g^{-1}]	RSD [%]	[µg g^{-1}]	RSD [%]
Na	Na^{23}	2217	33	183	26	2771	28
Mg	Mg^{25}	7381	25	5748	32	10360	19
Al	Al^{27}	43671	11	15203	31	83323	15
Si	Si^{29}	193715	11	332471	14	176003	18
P	P^{31}	11946	23	3284	24	20120	20
K	K^{39}	7718	27	4509	33	20368	24
Ca	Ca^{43}	36012	26	18895	31	16400	26
Ti	Ti^{47}	1098	23	444	35	3868	24
V	V^{51}	122	20	42	32	104	19
Cr	Cr^{53}	35	16	15	34	29	24
Mn	Mn^{55}	30078	18	81067	34	133323	33
Fe	Fe^{57}	229473	10	16306	31	76860	22
Co	Co^{59}	31	18	103	33	690	27
Ni	Ni^{60}	80	32	782	34	171	24
Cu	Cu^{63}	526	37	600	27	724	31
Zn	Zn^{67}	1114	22	1603	23	1249	33
Rb	Rb^{85}	22	23	18	34	96	23
Sr	Sr^{88}	272	36	369	28	571	23
Y	Y^{89}	153	13	40	24	113	20

Zr	Zr^{90}	26	24	34	22	235	26
Cs	Cs^{133}	1.2	34	0.74	28	16	26
Ba	Ba^{138}	1500	31	2021	36	9973	34
La	La^{139}	103	13	26	27	215	26
Ce	Ce^{140}	137	15	73	39	1425	32
Pr	Pr^{141}	26	13	8.9	34	55	25
Nd	Nd^{143}	120	14	39	33	200	25
Sm	Sm^{147}	27	15	8.9	27	39	21
Eu	Eu^{151}	3.5	14	2.4	33	7.5	21.6
Gd	Gd^{157}	29	15	10	27	34	22
Tb	Tb^{159}	3.9	14	1.6	32	4.8	22
Dy	Dy^{161}	25	13	8.5	29	28	23
Ho	Ho^{165}	5.2	13	1.6	27	5.1	21
Er	Er^{167}	16	14	4.5	36	16	21
Tm	Tm^{169}	2.2	13	0.51	22	1.9	22
Yb	Yb^{173}	14	16	3.4	24	13	23
Lu	Lu^{175}	2.2	17	0.57	27	1.9	22
Pb	Pb^{208}	182	17	311	42	1988	39
Th	Th^{232}	6.7	15	2.8	29	58	30
U	U^{238}	1.7	27	1.8	30	5.2	28

Table 5: Categorization of varnish types by structures and chemical composition

	Environment	Structures	Ce	Ba	Mn	Pb	Ce/Ce*	La_N/Yb_N	total REEs
Type I	arid deserts	mat-like layers, inter-mitted by mineral nests	+++	+++	++	++	+++	+++	+++
Type II	semi-arid to arid deserts	no layers	+++	+++	+++	++	+++	+++	+++
Type III	semi-arid deserts	no layers	+	+	+++	-	+	-	+
Type IV	urban areas	no layers	-	+	+	+++	-	+	-
Type V	river splash zones	discontinuous layers	-	+	-	-	--	-	+